The Planetary Science Journal, 7:88 (23pp), 2026 April https://doi.org/10.3847/PSJ/ae5244

A Portrait throughout Perihelion of the NH_2-rich Interstellar Comet 2I/Borisov

Sophie E. Deam[1,2], Michele T. Bannister[1], Cyrielle Opitom[3], Matthew M. Knight[4,5], Léa Ferellec[3], Ryan Ridden-Harper[1], Darryl Z. Seligman[6], Alan Fitzsimmons[7], Aurélie Guilbert-Lepoutre[8], Emmanuel Jehin[9], Laurent Jorda[10], Michael Marsset[11], Youssef Moulane[12], Philippe Rousselot[13], Pierre Vernazza[10], and Bin Yang[14]

[1] School of Physical and Chemical Sciences–Te Kura Matū, University of Canterbury, Private Bag 4800, Christchurch 8140, New Zealand; michele.bannister@canterbury.ac.nz
[2] Space Science and Technology Centre, School of Earth and Planetary Sciences, Curtin University, Perth, Western Australia 6845, Australia
[3] Institute for Astronomy, University of Edinburgh, Royal Observatory, Edinburgh EH9 3HJ, UK
[4] Physics Department, United States Naval Academy, 572C Holloway Road, Annapolis, MD 21402, USA
[5] University of Maryland, Department of Astronomy, College Park, MD 20742, USA
[6] Department of Physics and Astronomy, Michigan State University, East Lansing, MI 48824, USA
[7] Astrophysics Research Centre, School of Mathematics and Physics, Queen's University Belfast, Belfast BT7 1NN, UK
[8] Laboratoire de Géologie de Lyon, LGL-TPE, UMR 5276 CNRS / Université de Lyon / Université Claude Bernard Lyon 1 / ENS Lyon, 69622 Villeurbanne, France
[9] STAR Institute, Université de Liège, Allée du 6 août, 19C, 4000 Liège, Belgium
[10] Aix Marseille Univ, CNRS, LAM, Laboratoire d'Astrophysique de Marseille, Marseille, France
[11] European Southern Observatory, Alonso de Córdova 3107, Santiago, Chile
[12] School of Applied and Engineering Physics, Mohammed VI Polytechnic University, Ben Guerir 43150, Morocco
[13] Université Marie et Louis Pasteur, CNRS, Institut UTINAM (UMR 6213), OSU THETA, F-25000 Besançon, France
[14] Instituto de Estudios Astrofísicos, Facultad de Ingeniería y Ciencias, Universidad Diego Portales, Av. Ejército Libertador 441, Santiago, 8370191, Chile
Received 2025 July 7; revised 2026 March 2; accepted 2026 March 7; published 2026 April 22

Abstract

The interstellar comet 2I/Borisov is the first interstellar object where compositional characterisation was possible throughout its entire perihelion passage. We report all 16 epochs of a comprehensive optical observation campaign with ESO Very Large Telescope's integral field spectrograph MUSE, spanning 126 days from 2019 November 14 to 2020 March 19. The spatial dust emission of 2I/Borisov was predominantly smooth, with no seasonal effect. A jetlike feature was consistently visible. The gas production morphology of its coma was also smooth and similar for C_2, NH_2, and CN: symmetric around the optocentre. The production rates of these species gently declined into and beyond perihelion, until 2I's outburst and splitting event in early 2020 March. C_2, NH_2, and CN production rates all increased, with NH_2 being the most significant; the dust emission also slightly reddened. 2I/Borisov is a carbon-depleted, relatively NH_2-rich comet when compared to those comets yet measured in the solar system.

Unified Astronomy Thesaurus concepts: Interstellar objects (52)

1. Introduction

Interstellar objects (ISOs), interstellar interlopers (D. Jewitt & D. Z. Seligman 2023), or sola lapidae ("lonely rocks"; S. Portegies Zwart et al. 2018) are small bodies that originate from outside the solar system. The discovery of ISOs in the past eight years caused great excitement in the planetary community ('Oumuamua ISSI Team et al. 2019; A. Moro-Martín 2023; A. Fitzsimmons et al. 2024; D. Jewitt & D. Z. Seligman 2023; D. Z. Seligman & A. Moro-Martín 2023).

Classically, ISOs are inferred to be remnants of the planetesimal formation process. Their physical properties could therefore help us constrain aspects of the disk chemistry and planetary architecture of their origin system (A. Miotello et al. 2023). These small bodies are ejected into interstellar space, for instance by gravitational scattering from other bodies in the disk (S. N. Raymond et al. 2018; A. C. Childs & R. G. Martin 2022), the stellar cluster (T. O. Hands et al. 2019; S. Pfalzner et al. 2021), or later post-main-sequence unbinding (e.g., W. G. Levine et al. 2023), and orbit in the Galaxy (J. C. Forbes et al. 2025). A tiny fraction of the vast galactic ISO population continuously passes through the solar system's observable volume, where they can be identified and characterized with the same techniques as small bodies native to the solar system. ISOs provide an opportunity to directly sample other planetary systems, comparing the outcomes of planetesimal formation both in our solar system and in distant systems.

Of the first two known macroscopic ISOs, 1I/'Oumuamua (G. V. Williams et al. 2017) and 2I/Borisov, discovered in 2019 August,[15] only the second had a detectable coma, helpful for chemistry characterization of internal material previously shielded from interstellar medium processing. 1I/'Oumuamua generated intense discussion, due to its lack of a detectable coma, but moderate radial (or antisolar) nongravitational acceleration (M. Micheli et al. 2018), and high-amplitude light curve, which implied an unusually high-aspect ratio 6:1 shape with an oblate geometry (S. Mashchenko 2019). In contrast, 2I/Borisov had an extended coma already visible at the time of detection and in precovery data (Q. Ye et al. 2020). 2I/Borisov's unbound orbit has an eccentricity of 3.36, a perihelion distance of 2.01 au, and a closest approach date of 2019 December 8.

Like solar system comets, 2I underwent post-perihelion changes. Two outbursts were detected between 2020 March 4 and 9 (M. Drahus et al. 2020), resulting in a total brightness

[15] *Minor Planet Electronic Circular* 2023-U162.

increase of 2I by 0.7 mag over the 5 days. The March outbursts coincided with a splitting of the nucleus, confirmed when the fragment became resolvable by the Hubble Space Telescope (HST) on 2020 March 30 (D. Jewitt et al. 2020). The splitting involved the ejection of a fragment with a mass of around 0.01% of the nucleus.

2I/Borisov exhibited many traits with strong similarities to solar system comets. Color measurements showed that the dust was redder than the Sun (P. Guzik et al. 2020; J. de León et al. 2020; M.-T. Hui et al. 2020; T. Kareta et al. 2020; A. Fitzsimmons et al. 2019; B. Yang et al. 2020, 2021; E. Mazzotta Epifani et al. 2021), and the coma was dust-rich with properties similar to those of 67P/Churyumov–Gerasimenko (67P; V. V. Busarev et al. 2021). The coma's structure at discovery showed features similar to jets, with two enhancements that were generally perpendicular to the solar direction (B. T. Bolin & C. M. Lisse 2020; F. Manzini et al. 2020; E. Mazzotta Epifani et al. 2021). Radio observations of 2I using occultation and interplanetary scintillation techniques found small-scale density structures in the range of ∼10–70 km in the plasma tail (P. K. Manoharan et al. 2022). Spectroscopic measurements showed further similarity to solar system comets, with an early detection of CN (A. Fitzsimmons et al. 2019) and later C_2 emission at optical wavelengths. C_2 was depleted relative to CN, like the "carbon-depleted" group (A. Fitzsimmons et al. 2019; C. Opitom et al. 2019b; M. T. Bannister et al. 2020; T. Kareta et al. 2020; H. W. Lin et al. 2020; K. Aravind et al. 2021). Higher-resolution spectroscopy revealed gaseous nickel (P. Guzik & M. Drahus 2021), and a comparable NiI/FeI abundance ratio and ammonia ortho-to-para ratio (C. Opitom et al. 2021).

However, 2I/Borisov was unusual relative to almost all solar system comets in one respect; it was extremely rich in CO relative to HCN and water (D. Bodewits et al. 2020; M. A. Cordiner et al. 2020). The only comet with a coma richer in CO than 2I to date is C/2016 R2 (N. Biver et al. 2018). This high CO measurement was corroborated by the high ratio of the green-to-red doublet intensity of the three [O I] forbidden oxygen lines measured by C. Opitom et al. (2021), which has been suggested to indicate a significant contribution of CO or CO_2 (A. McKay et al. 2024) to the outgassing compared to H_2O.

These properties have influenced the discussion of the environment in which 2I could have formed and its subsequent evolution. Based on its high CO abundance, M. A. Cordiner et al. (2020) and D. Bodewits et al. (2020) argued that 2I probably originated outside the CO line of its home planetary disk. There is also the possibility that 2I is an outer fragment of a larger-differentiated object, as proposed for C/2016 R2 (N. Biver et al. 2018). S. Bagnulo et al. (2021) argued that the homogeneous, high degree of polarization of 2I in comparison to solar system comets indicates it had not passed close to any star since its formation (see also P. Halder & S. Sengupta 2023). As post-ejection stellar encounters are unlikely (J. C. Forbes et al. 2025), one can infer that any thermal alteration of 2I, which is minimal, occurred in its host system and is strongly connected to its dynamical history.

The high velocities of ISOs (M. J. Hopkins et al. 2025) mean that the period during which their spectroscopic characterization is possible is brief, predicted to be a few hundred days if found when inbound (R. C. Dorsey et al. 2025). For 1I, detected post-perihelion, only a few weeks of observation were possible for most facilities before it grew too faint. Extensive multimonth datasets of major facility characterization could not be acquired with anything other than HST (see, e.g., D. Jewitt & D. Z. Seligman 2023). In contrast, 2I/Borisov was the first ISO detected pre-perihelion. Upon discovery at a heliocentric distance of 2.98 au, its brightness was sufficient for characterization with 8 m class ground-based telescopes.

We conducted an extensive observing campaign of 2I/Borisov through its perihelion passage with ESO Very Large Telescope (VLT)'s Multi Unit Spectroscopic Explorer (MUSE) from 2019 November 14 onward. Due to the COVID-19 pandemic and associated closure of telescopes to safeguard the health of all involved, the program ended earlier than the limiting magnitude of MUSE, on 2020 March 19—the last observation made of this interstellar comet with a major ground-based facility.[16] The initial results of the gas production rates of C_2, NH_2, and CN and dust continuum slope for the 2019 November 14, 15, and 26 observations were reported in M. T. Bannister et al. (2020).

Here, we report on the MUSE dataset from the entire 126 day span of the observing campaign. With a new star-subtraction package for integral field unit (IFU) spectrographs, built specifically to account for the dense stellar fields that 2I moved across (`starkiller`, R. Ridden-Harper et al. 2025; Section 3.2), we study the spatial distribution of 2I's outgassing with maps of the solar reflectance gradients (Section 4.1) and dust (Section 4.2). We assess spatial gas emission (Section 4.3) and compute gas production rates through the perihelion passage of 2I and beyond (Section 4.4). Finally, we consider the variability of 2I and its aspects of unusual composition relative to solar system comets (Section 5).

2. Observations

2I/Borisov was observed with ESO VLT's MUSE from 2019 November 14 to 2020 March 19, under the ESO Director's Discretionary programs 103.2033.001–003 and Normal program 105.2086.002. The campaign acquired 16 epochs, which are summarized in Table 1. Figure 1 illustrates 2I's trajectory through the solar system and the extensive portion of its journey covered by MUSE observations. All observations, including reduced data products, are publicly available,[17] with analysis scripts also available.[18]

MUSE operates on the Nasmyth platform of the 8.2 m diameter optical telescope UT4 at ESO's Paranal Observatory in Chile. This instrument has a large field of view (FOV; $1' \times 1'$) covered by 24 individual IFUs, ideal for imaging extended sources (R. Bacon et al. 2010). The nominal MUSE wavelength range spans 4830–9300 Å, with a spatial sampling of $0\farcs2 \times 0\farcs2$ and spectral resolution of 1.25 Å. This covers the emission bands of the Swan $C_2(\Delta v = 0,\ \Delta v = 1)$ system, several amino radical NH_2 bands, and the red CN $A^2\Pi$–$X^2\Sigma^+$ system. MUSE was used in the wide-field mode without adaptive optics for all of the observations reported in this paper. At each epoch, 2I/Borisov was imaged for 4×600 s

[16] The last ground-based observation of 2I reported to the Minor Planet Center was astrometry from New Zealand's Mt John Observatory in Takapō, 2020 April 28, when New Zealand returned to Covid-19 Alert Level 3.

[17] doi: 10.11570/26.0006

[18] https://github.com/sed79/super-duper-comet

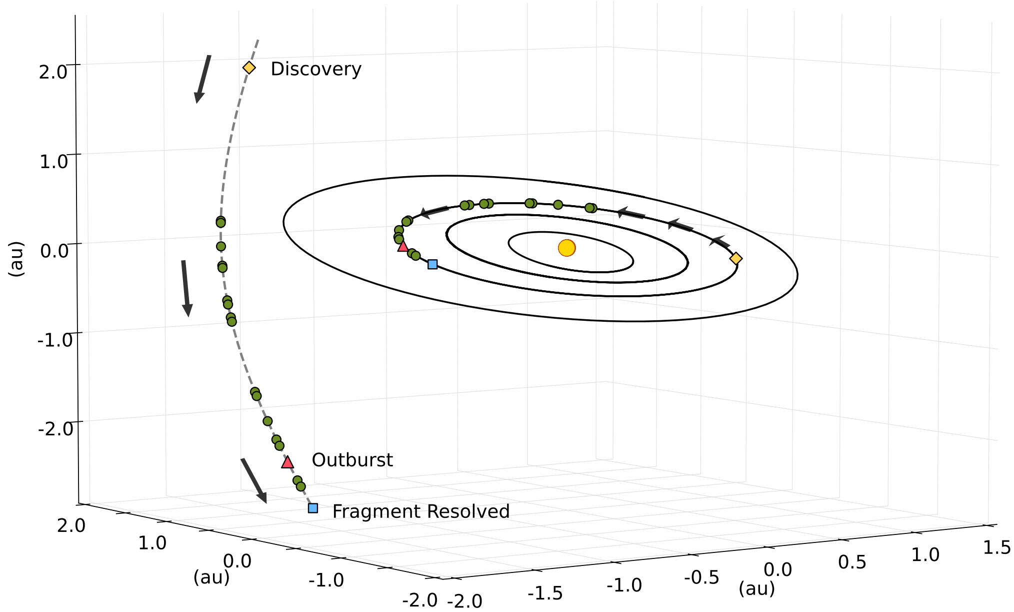

Figure 1. Relative positions of 2I/Borisov and other solar system bodies during the VLT/MUSE observing campaign, shown in International Celestial Reference Frame coordinates at the scale of astronomical units (au). The trajectory of 2I follows the dashed line in the direction of the arrows. Green circles indicate the positions of 2I and Earth at each of the 16 observing epochs (Table 1). Colored symbols are additional events identified independent of our data: yellow diamonds represent 2I and Earth's positions at discovery on 2019 August 30, orange triangles the outburst of 2020 March 4–9 (M. Drahus et al. 2020), and blue squares when the fragment was resolved by HST on 2020 March 30 (D. Jewitt et al. 2020). The black lines outward from the Sun (yellow circle) are the orbits of Mercury, Venus, Earth, and Mars.

Table 1
VLT/MUSE Observations of 2I/Borisov, with Geometric Relationships between 2I, Earth, and the Sun

Observation Date (UTC)	N[1]	Airmass[2]	Seeing[3] (arcsec)	r_h^4 (au)	Δ^5 (au)	Elongation[6] (deg)	α^7 (deg)	$\theta^8_{-\odot}$ (deg)	θ^9_{-V} (deg)	l^{10} (km)
2019 Nov 14 08:03-08:48	4[a]	2.17	0.8	2.08	2.23	68.25	26.26	289.29	330.98	1617
2019 Nov 15 08:02-08:53	4[a]	2.13	0.87	2.07	2.22	68.60	26.40	289.25	330.94	1608
2019 Nov 26 07:17-08:03	4	2.16	0.43	2.02	2.09	72.41	27.69	289.11	330.02	1517
2019 Dec 5 07:09-07:55	4	1.82	0.93	2.01	2.02	75.40	28.36	289.50	328.65	1462
2019 Dec 6 07:37-08:25	4[b]	1.55	1.04	2.01	2.01	75.73	28.42	289.57	328.45	1457
2019 Dec 21 07:56-08:13	4[a]	1.21	0.49	2.03	1.94	80.39	28.60	291.52	324.50	1410
2019 Dec 23 05:50-06:42	4	1.98	0.39	2.03	1.94	80.96	28.55	291.89	323.84	1407
2019 Dec 29 05:18-06:09	4	2.12	0.66	2.06	1.94	82.74	28.30	293.22	321.54	1405
2019 Dec 31 05:36-06:22	4	1.83	0.41	2.07	1.94	83.33	28.18	293.74	320.68	1406
2020 Feb 2 04:17-05:03	4	1.66	0.45	2.35	2.08	93.18	24.71	307.01	302.04	1512
2020 Feb 4 03:18-04:05	4[c]	2.01	0.55	2.38	2.10	93.81	24.44	308.12	300.82	1522
2020 Feb 16 04:07-05:04	5[d]	1.53	0.6	2.53	2.20	97.83	22.77	315.86	293.87	1593
2020 Feb 25 03:28-04:11	4	1.57	0.81	2.65	2.28	101.03	21.49	322.76	289.78	1653
2020 Feb 28 04:02-04:48	4[e]	1.45	0.72	2.70	2.31	102.14	21.06	325.32	288.69	1674
2020 Mar 16 04:41-05:28	4[f]	1.33	1.23	2.96	2.48	108.59	18.61	341.85	285.55	1801
2020 Mar 19 05:23-06:14	4[e]	1.31	0.61	3.00	2.52	109.74	18.19	345.14	285.50	1826

Notes. (1) Number of frames, (2) starting airmass, (3) FWHM seeing value at the beginning of the observation measured by the ASM-DIMM telescope, (4) heliocentric distance, (5) geocentric distance, (6) solar elongation angle, (7) solar phase angle, (8) position angle of the antisolar direction, (9) position angle of the negative velocity vector, (10) physical size of 1" projected to the distance of 2I in kilometers.
[a] Two frames were discarded due to a high twilight background.
[b] One frame was discarded due to a high twilight background.
[c] Three frames were omitted from the production rate analysis due to 2I passing in front of a star.
[d] One frame was discarded due to thin cloud conditions.
[e] One frame was discarded, and one frame was omitted from the production rate analysis due to 2I passing in front of a star.
[f] Two frames were omitted from the production rate analysis due to 2I passing in front of a star.

exposures. Interjecting sky exposures were obtained after the first and third images, intended to be used for clear sky measurements, but ended up not being used in the analysis (see Section 3). Sky exposures were integrated for 180 s during epochs 2019 November 14 through to 2020 February 4, and were reduced to 120 s for 2020 February 16 onward, because the field surrounding 2I became increasingly crowded as the comet passed into the plane of the Milky Way. Small dithering and 90° rotation were applied between each of the four target exposures to allow for the removal of detector signatures.

Standard stars were observed each night to flux-calibrate the data (Appendix A).

The 2019 November 14 images are off-center within the FOV due to ephemeris uncertainties[19] that were subsequently resolved. Observations on all nights except 2020 February 16 were made in clear or photometric conditions (Table 1). The third exposure obtained that night was affected by clouds, so an additional exposure was acquired and the affected exposure discarded. However, the extra image does not have the same rotation orientation as the image it was replacing, so the detector signals were not as efficiently removed after coadding. The strong background from morning twilight and the close proximity of background stars prevented us from using a number of exposures (see Appendix A).

3. Data Reduction and Analysis

3.1. Initial Data Reduction

The MUSE data reduction pipeline (P. M. Weilbacher et al. 2020) performed dark subtraction, flat-fielding, telluric correction, flux calibration, and data cube reconstruction. Data cubes were sky-subtracted in two different ways: using in-frame sky measurements and offset sky exposures. For the first sets of observations on November 14 and 15, we used the in-frame sky measurements for subtraction, as the scientific exposures of 2I were taken deep in twilight and suffered from a significant and varying sky background. In theory, using in-frame sky measurement could lead to an oversubtraction of the sky if the object occupies a significant portion of the FOV. For these observations, we performed tests with the two different sky techniques, comparing the production rates derived, and did not find any sign of oversubtraction when using in-frame sky measurements. We thus decided to use that technique for the entire dataset. The output cubes were made with wavelength calibration to arc line wavelengths in air (as opposed to vacuum), as is the default for the MUSE reduction pipeline.

Telluric absorption was dealt with in two different ways. For creating maps of the gas and dust, we used the pipeline telluric correction, based on observations of the standard stars. Since the standard stars were not observed at the same time or at the same airmass as the object, this method can under- or overcorrect the telluric absorption. This is not a problem when looking at gas maps, but it is more critical when deriving CN production rates, since that region of the spectrum is significantly affected by telluric absorptions. For the purpose of deriving production rates, we therefore skipped the pipeline telluric correction and performed it directly on the extracted spectra using the Molecfit software (A. Smette et al. 2015).

3.2. Map Creation

Maps of 2I's continuum, solar reflectance, and emission of the radicals CN, C_2, and NH_2 were created using data cubes obtained in photometric or clear conditions (with the exception of 2020 February 16; see Table 1). 2I's passage in front of the galactic plane during the post-perihelion observations meant up to ∼400 stars of 21st magnitude in GAIA-G and brighter were present in a single exposure.

Due to the increasingly numerous stars in the FOV, the observations on and after 2019 December 31 were processed with a tool named `starkiller`,[20] specifically developed to remove streaked sources in IFU data cubes (R. Ridden-Harper et al. 2025). Each data cube was passed to `starkiller` individually before extracting or combining maps. The removal of streaks overlapping with 2I's coma allowed an extra four data cubes to be included in the map creation, where stellar contamination had initially led to discarding them. Only two exposures were discarded because the stars behind 2I could not be sufficiently removed. `starkiller` also improved the image quality derived from a further 27 data cubes.

A comparison of maps created from data cubes processed with and without `starkiller` is reproduced from R. Ridden-Harper et al. (2025) in Figure 2. The quality of the star subtraction is wavelength-dependent, due to pipeline processes that keep the subtraction as unbiased as possible. This means that the subtraction quality varies between the maps produced here. It was more effective in the CN range than the dust images in Figure 2. `starkiller` was most successful when it prevented a star-contaminated exposure from being discarded to increase the number of frames being coadded together and the overall signal-to-noise ratio (SNR) of the final data product, such as 2020 February 4 and 2020 March 19.

After the star removal, the extreme pixel values (upper and lower 5×10^{-6} percentiles) caused by cosmic rays and other sources of noise were masked. The comet's optocentre (center of brightness) was determined with the `photutils` 2D Gaussian centroid algorithm. To spatially align each data cube and place 2I consistently in the center, a uniform shift was applied to each image slice using third-order spline interpolation with `MUSE Python Data Analysis Framework` (`MPDAF`; R. Bacon et al. 2016).

3.2.1. Dust and Color Maps

Dust maps were extracted by collapsing aligned data cubes in the spectral dimension over 7080–7120 Å (Table 2), a wavelength range that contains few gas or sky emission lines (T. L. Farnham et al. 2000). Inspecting the maps, we do not see any sign of rotation by 2I. We stacked the observations from a single night obtained over 1 hr, and additionally stacked together 2019 December 5–6, which were only 24 hr apart, to increase the SNR of the data when investigating coma structure. The physical scale in the image changed between December 5 and 6 as the distance from the Earth to 2I decreased. In other words, although the images were aligned at the coma center, coma features were misaligned by up to 200 km at the image edge, which we did not adjust for before coadding between dates. We justified this decision by verifying that the relevant features—or lack thereof—were evident in the exposures from individual nights, i.e., the coadding does not affect our interpretation.

In order to create maps of the dust color, each data cube was also divided by a reference solar spectrum (M. Meftah et al. 2018), which was interpolated using `scipy.interpolate` to match the data cube's spectral sampling. Three wavelength ranges of width 40 Å were extracted from regions of each data cube without gas emission, and then averaged along the

[19] The ephemerides from IMCCE differed from those from JPL Horizons. Subsequent observations only used Horizons.

[20] Commit da0b884: https://github.com/CheerfulUser/starkiller.

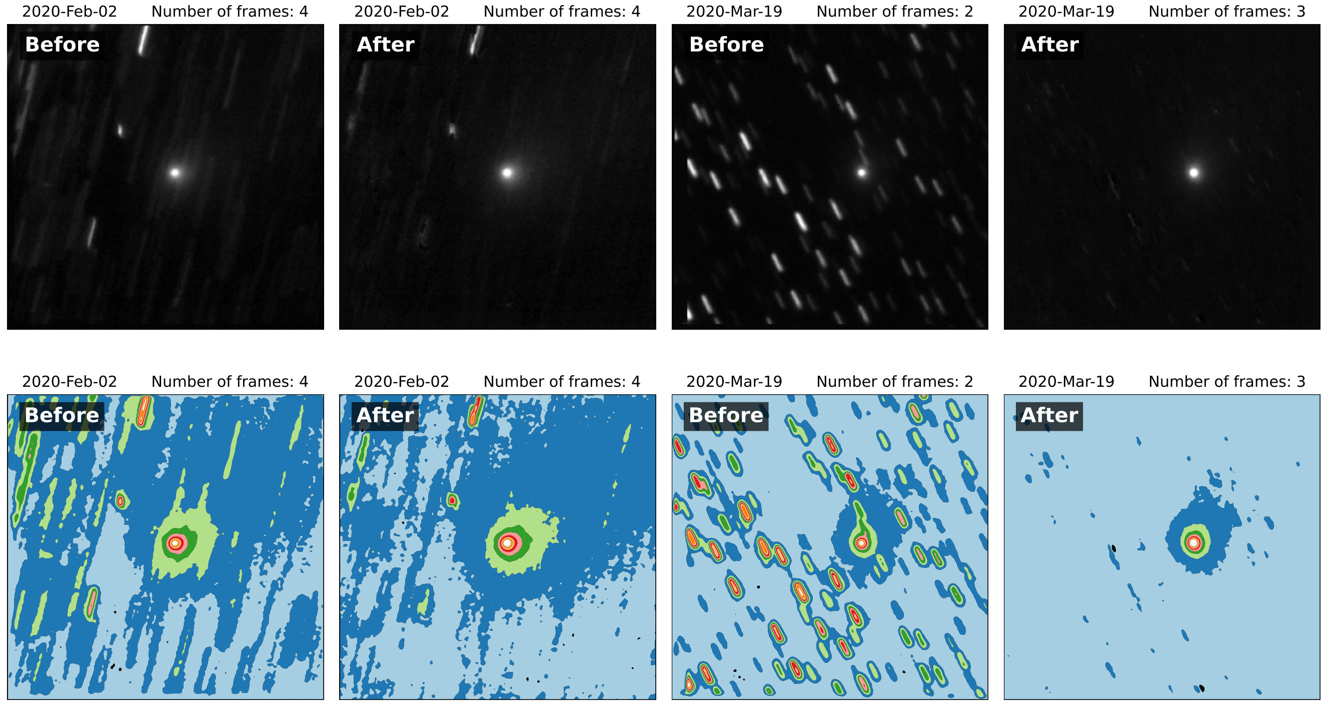

Figure 2. Images of the dust emission (7080–7120 Å) from 2I/Borisov before and after the application of the `starkiller` pipeline. 2I was within 10 degrees of the Galactic plane on 2020 February 2 and 2020 March 19, and the FOV for each exposure contained between 80 and 136 stars brighter than 21st magnitude in GAIA-G. More significant improvement occurred for the 2020 March 19 data: the number of usable exposures (without a star directly behind 2I) increased from 2 to 3 due to `starkiller`, allowing for improved median coadding and the removal of more stars. Both rows show the maps with a square root stretch, and the contour levels in the bottom row illustrate the reduction of star flux to below the signal from the coma.

Table 2
Electronic Transitions and Corresponding Wavelength Ranges Used to Extract Maps from MUSE Data Cubes

Species	System	Transition	Wavelengths (Å)
Dust	⋯	⋯	7080–7120
C_2	$d^3\Pi_g$–$A^3\Pi_u$	$(\Delta\nu = 0)$	5075–5171
NH_2	$\tilde{A}^2A_1 - \tilde{X}_1^{2B}$	(0,9,0)–(0,0,0)	5973–5982
NH_2	$\tilde{A}^2A_1 - \tilde{X}_1^{2B}$	(0,9,0)–(0,0,0)+[O^{1}D]	5991–6001
NH_2	$\tilde{A}^2A_1 - \tilde{X}_1^{2B}$	(0,9,0)–(0,0,0)	6016–6026
NH_2	$\tilde{A}^2A_1 - \tilde{X}_1^{2B}$	(0,8,0)–(0,0,0)	6330–6340
CN	⋯	(1–0)	9135–9210

Note. Each wavelength range for NH_2 was combined into a single map.

spectral dimension to produce three maps centered around the wavelengths 5280, 7080, and 8600 Å. The 7080 Å map was used to study the dust morphology, while the other two were used to produce color maps.

The normalized reflectivity gradient was calculated for each pixel using the definition of D. Jewitt & K. J. Meech (1986),

$$S'(\lambda_1, \lambda_2) = (dS/d\lambda)/S_{\mathrm{mean}}, \quad (1)$$

where λ_1, λ_2 are the wavelengths 5280 and 8600 Å, S is the solar divided spectrum such that $dS/d\lambda$ is the gradient of S over 5280–8600 Å, and S_{mean} is the mean within the wavelength range 5280–8600 Å, for which we substitute the average flux around 7080 Å because it avoids emission bands and best represents the continuum. Where $S_{\mathrm{mean}} = 0$, S' was simply set to zero to avoid division by S_{mean}. Color maps were stacked in the same way as dust maps. The median value and root-mean-square error of S' within a 5000 km diameter aperture were calculated from the maps to report a single S' value for each night. To assess any changes in S' after the reported March outburst, a linear regression line was fitted to the data preceding the outburst that was weighted by the measurement uncertainties. The post-outburst data were then compared with the 95% or 2σ prediction confidence interval for the corresponding dates to conclude whether there was a statistically significant change.

3.2.2. Gas Emission Maps

To isolate the spectrum of 2I's gas emission, the light scattered by the dust in the coma was removed from the data cubes by subtracting a spectrum of comet 67P, previously obtained by MUSE (A. Guilbert-Lepoutre et al. 2016; C. Opitom et al. 2020), which does not contain any gas emission. First, to account for differences in the dust color caused by phase angle and composition (expected between 2I and 67P), the spectrum of 2I was divided by the 67P spectrum at each spatial location of a data cube. A second-order polynomial was then fitted to the resulting spectrum over regions containing no gas emission, to produce a model polynomial. This was used to weight and slope correct the spectrum of 67P to match the gradient of 2I. The 67P spectrum was then normalized and subtracted from each 2I spectrum to produce dust-subtracted data cubes. As the same subtraction technique was applied to all spatial locations within the data cube, the remaining stars in the FOV after removal by `starkiller` also had a spectrum of 67P subtracted from them. This led to oversubtraction or undersubtraction, since these stellar spectra have different colors and features from

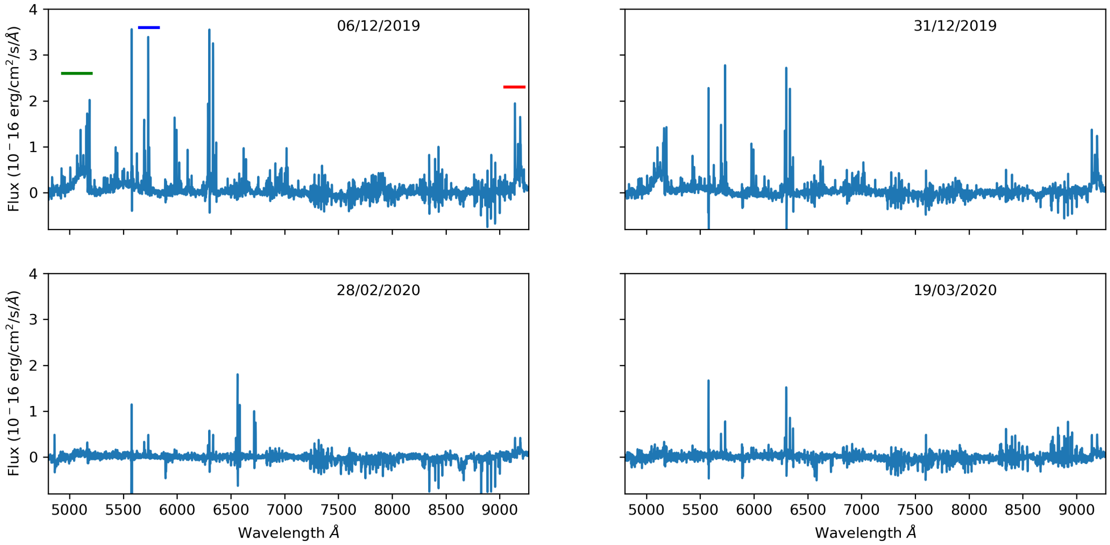

Figure 3. Dust-subtracted spectra of 2I at four different dates, extracted within a 5000 km radius, over the wavelength range captured by MUSE and displayed in Angstroms (Å). The C_2, NH_2, and CN bands used to measure production rates are indicated by the green, blue, and red lines, respectively.

67P, meaning that the stars in the gas maps appear as either dark or light streaks. Due to the proximity of the CN(1–0) emission at 9109 Å to MUSE's upper limiting wavelength at 9300 Å, there existed a "dip feature" in the continuum of each spectrum that did not exist in the spectrum of 67P. The spectra in each data cube were further manually flattened over the region 8800–9300 Å by applying a seventh-order polynomial to a coadded spectrum with a well-defined "dip feature" to be used as a model continuum for scaling and subtraction from each spatial pixel's spectrum, creating a flat continuum under the CN emission.

Gas maps were extracted by collapsing the data cubes in the spectral dimension over the wavelength ranges outlined in Table 2. All regions extracted covering NH_2 emission were combined into a single image. Gas maps from different data cubes were stacked following the same procedure as for the dust.

3.3. Image Enhancement

The technique of subtracting the azimuthal median was used to investigate the nonuniformity of the coma around the optocentre of 2I. Areas of the coma with enhancement values significantly above and below zero indicate potential morphological features, whereas an image with enhancement values close to zero indicates a uniform coma. For more examples of the technique, we direct the reader to M. M. Knight et al. (2017).

3.4. Gas Production Rates

To derive production rates, we extracted spectra over the same physical aperture of 5000 km for each data cube. This aperture size is rather small compared to what is usually used to measure gas production rates, but was chosen to avoid stars contaminating the extracted spectra in the 2020 observations, when 2I was crossing a crowded field. Note that `starkiller` was not applied to the data cubes used in gas production rate measurements: reducing the aperture radius was generally sufficient to avoid stellar contamination in these measurements, and on rare occasions when it was not, we note it in Appendix A.

The extracted spectra for each epoch were then averaged to increase the SNR. The telluric signatures were corrected using the Molecfit software (A. Smette et al. 2015), and the continuum contribution was subtracted. For continuum subtraction, we used a spectrum of comet 67P obtained from MUSE data (containing only the dust signature; A. Guilbert-Lepoutre et al. 2016; C. Opitom et al. 2020), whose slope was adjusted to match the slope of 2I in each observation, similar to what was done to produce the gas maps. Examples of dust-subtracted spectra are shown in Figure 3.

In the resulting spectra, emissions from the $C_2 \delta\nu = 0$ and $\delta\nu = 0$–1 bands, the NH_2 A–X (0,10,0)–(0,0,0), (0,9,0)–(0,0,0), (0,8,0)–(0,0,0), and (0,7,0)–(0,0,0) bands, and the red CN (1–0) band around 9140 Å are clearly visible. As 2I/Borisov moved away from the Sun in 2020, fainter bands progressively became undetectable in our observations. However, the $C_2 \delta\nu = 0$, NH_2 A–X (0,10,0)–(0,0,0), and CN (1–0) bands remained detectable throughout our campaign and were used to measure gas production rates.

To derive the gas production rates, we measured the flux in each band for each epoch, using the continuum-subtracted spectra. For CN, we simply integrated the spectra over the 9100—9270 Å range. The CN (1–0) band contains flux at longer wavelengths, but we limited the integration to that range to avoid telluric and second-order contamination at longer wavelengths. We then multiplied the flux by a factor of 1.4 to account for the missing flux (U. Fink 2009). For the $C_2 \delta\nu = 0$ band, we integrated the flux over the 4800–5170 Å range. For NH_2, we adjusted a set of Gaussians to reproduce the peaks of the (0,10,0)–(0,0,0), and then integrated them to obtain the total flux in the band, in addition to simply integrating the flux over the wavelength range of the band. Both techniques resulted in similar fluxes being measured.

In parallel, we used the Planetary Spectrum Generator (PSG; G. L. Villanueva et al. 2018) to retrieve synthetic spectra that match the relative intensities of the bands observed for 2I. The synthetic spectra matched well the shape and intensity of the bands we observed, without noise produced by

Table 3
Molecular Fluorescence Efficiencies and Haser Model Scale Lengths for Parent and Daughter Species l_p, l_d at $r_H = 1$ au

Band	g (erg s^{-1} mol^{-1})	l_p (km)	l_d (km)
$C_2(\Delta v = 0)$	4.5×10^{-13}	2.2×10^4	6.6×10^4
NH_2(0,10,0)	9.2×10^{-15}	4.1×10^3	6.2×10^4
CN(1–0)	8.85×10^{-14}	1.3×10^4	2.1×10^5

Note. g-factors for C_2 are from M. F. A'Hearn et al. (1995), for CN from Y. Shinnaka et al. (2017), and for NH_2 from C. Arpigny (1994). g-factors are assumed to scale as r_H^{-2} and scale lengths as r_H^2. Scale lengths are from M. F. A'Hearn et al. (1995) for C_2 and CN, and from A. L. Cochran et al. (2012) for NH_2. Used with $v = 0.5$ km s^{-1}.

the sky and continuum subtraction. However, while C_2 production rates could be retrieved and matched closely with those measured with the technique described above, production rates provided by the PSG retrieval were inconsistent with the production rates derived using the method described above for CN, potentially because of different models and model parameters used, and did not contain NH_2. We thus used the synthetic spectra to measure the flux in the CN and C_2 as for our observed spectra.

We converted the measured fluxes to column densities using the fluorescence efficiencies given in Table 3 and used a Haser model (L. Haser 1957) to derive gas production rates. We used a velocity of 0.5 km s^{-1} and the scale lengths listed in Table 3. We used a velocity of 0.5 km s^{-1} to enable easier comparison with the values in M. T. Bannister et al. (2020). We primarily selected scale lengths from M. F. A'Hearn et al. (1995), as it, along with later work by A. N. Bair & D. G. Schleicher (2025) using similar parameters, represents the largest database of CN and C_2 measurements of comets in the literature. However, they do not provide scale lengths for NH_2, so we used scale lengths from A. L. Cochran et al. (2012) for this. The scale length used can affect the measured production rates significantly, as demonstrated by L. Ferellec et al. (2024), for example. We thus also provide the measured fluxes in the manuscript so that the reader can recompute the production rates using their preferred parameters. We computed gas production rates using both the fluxes measured in our observed spectra and in our modeled spectra, which were consistent with each other. The production rates reported in Table 4 are based on modeled spectra for CN and C_2, and the set of Gaussians for NH_2, with the uncertainties estimated from the variation between the production rates derived from observed and modeled spectra. This uncertainty reflects the dominant contribution of the continuum subtraction and telluric correction in the gas production rate measurement.

To test for any significant changes in the production rates and their ratios from the splitting of the nucleus, we fitted a trend to the post-perihelion data obtained prior to the March outburst, with the same method as for the dust color described in Section 3.2.1.

4. Results

4.1. Dust Color

The normalized solar reflectance gradient maps S' within 5280–8600 Å are shown in Figure 4. 2I's color ranges from 4%/1000 Å to 10%/1000 Å and does not vary significantly

Table 4
Fluxes and Production Rates of the C_2, NH_2, and CN Gas Emission of 2I/Borisov

Date (UTC)	Flux (10^{-15} erg s^{-1} cm^{-2}) C_2	NH_2	CN	Production Rate (10^{24} mol s^{-1}) $Q(C_2)$	$Q(NH_2)$	Q(CN)
2019 Nov 14	5.75	2.86	6.59	0.72 ± 0.2	4.9 ± 0.8	2.4 ± 0.2
2019 Nov 26	6.34	3.44	7.43	0.65 ± 0.3	4.8 ± 0.8	2.2 ± 0.2
2019 Dec 5	6.89	3.33	7.81	0.64 ± 0.3	4.2 ± 0.8	2.1 ± 0.2
2019 Dec 6	7.09	3.47	7.64	0.65 ± 0.2	4.4 ± 0.5	2.0 ± 0.2
2019 Dec 21	5.94	2.84	7.29	0.53 ± 0.2	3.4 ± 0.5	1.9 ± 0.2
2019 Dec 23	5.75	2.88	6.34	0.51 ± 0.2	3.5 ± 0.7	1.7 ± 0.2
2019 Dec 29	5.21	2.78	…	0.48 ± 0.2	3.5 ± 0.4	…
2019 Dec 31	5.23	2.57	5.70	0.49 ± 0.2	3.3 ± 0.5	1.6 ± 0.2
2020 Feb 2	1.59	1.01	2.81	0.27 ± 0.2	2.3 ± 0.1	1.5 ± 0.2
2020 Feb 4	1.79	1.29	2.85	0.32 ± 0.2	3.0 ± 0.1	1.6 ± 0.2
2020 Feb 16	0.87	0.37	2.35	0.21 ± 0.2	1.2 ± 0.1	1.7 ± 1.0
2020 Feb 25	0.92	0.53	2.04	0.28 ± 0.2	2.1 ± 1.0	1.8 ± 0.7
2020 Feb 28	0.92	0.56	1.59	0.31 ± 0.2	2.4 ± 1.0	1.6 ± 0.7
2020 Mar 16	1.12	0.64	1.75	0.60 ± 0.5	4.4 ± 1.0	2.8 ± 1.5
2020 Mar 19	0.73	0.73	1.58	0.43 ± 0.3	5.4 ± 1.0	2.7 ± 1.5

Note. Exposures from 2019 November 14 and 2019 November 15 were combined before the production rates were calculated. Observations from 2019 December 29 had additional telluric contamination over the CN wavelengths that were difficult to remove, so we do not report values for this date.

through time over the MUSE observations. The dust appears redder in the center and bluer farther out in the coma. This has been seen previously, e.g., for C/2016 ER61 (C. Opitom et al. 2019a), and is consistent with particle size sorting where larger ("redder") particles occupy the central part of the coma, and smaller ("bluer") particles occupy the outer regions of the coma. In most maps, we see a significantly redder central part, which could point to a condensed inner coma made of larger particles. The sky and background stars are plotted as white, either due to extreme slopes for stars or division by small sky fluxes around 7080 Å. The noise produced by the division of low flux around 7080 Å was not mitigated or masked for the risk of altering the boundary between 2I and the sky. For nights with only two stacked observations (see Appendix A), residual stellar contamination remains in Figure 4 even after `starkiller` subtraction, where white pixels (values outside the color bar range) are close to the comet. The subtracted stars were never directly behind the comet, however, so the contamination does not alter the aperture-measured S' values and is adequately captured by the uncertainties.

The dust color over the 5000 km diameter aperture extracted from MUSE data is consistent with other photometric methods, illustrated in Figure 5 (see also a summary in Appendix B). S' is lower than other measurements taken in the visible; however, the range 5280–8600 Å used here extends further into the near-IR. This is consistent with the concept of a lower solar reflectance gradient at longer wavelengths of dust (D. Jewitt & K. J. Meech 1986), but makes it challenging to compare between datasets measured in different wavelength ranges.

E. Mazzotta Epifani et al. (2021) measured the reddening of 2I between the Bessel R and I filters over multiple annuli at increasing distances from the optocentre (2×10^3 km through to 1.3×10^4 km), and found a decreasing slope, i.e., reddening

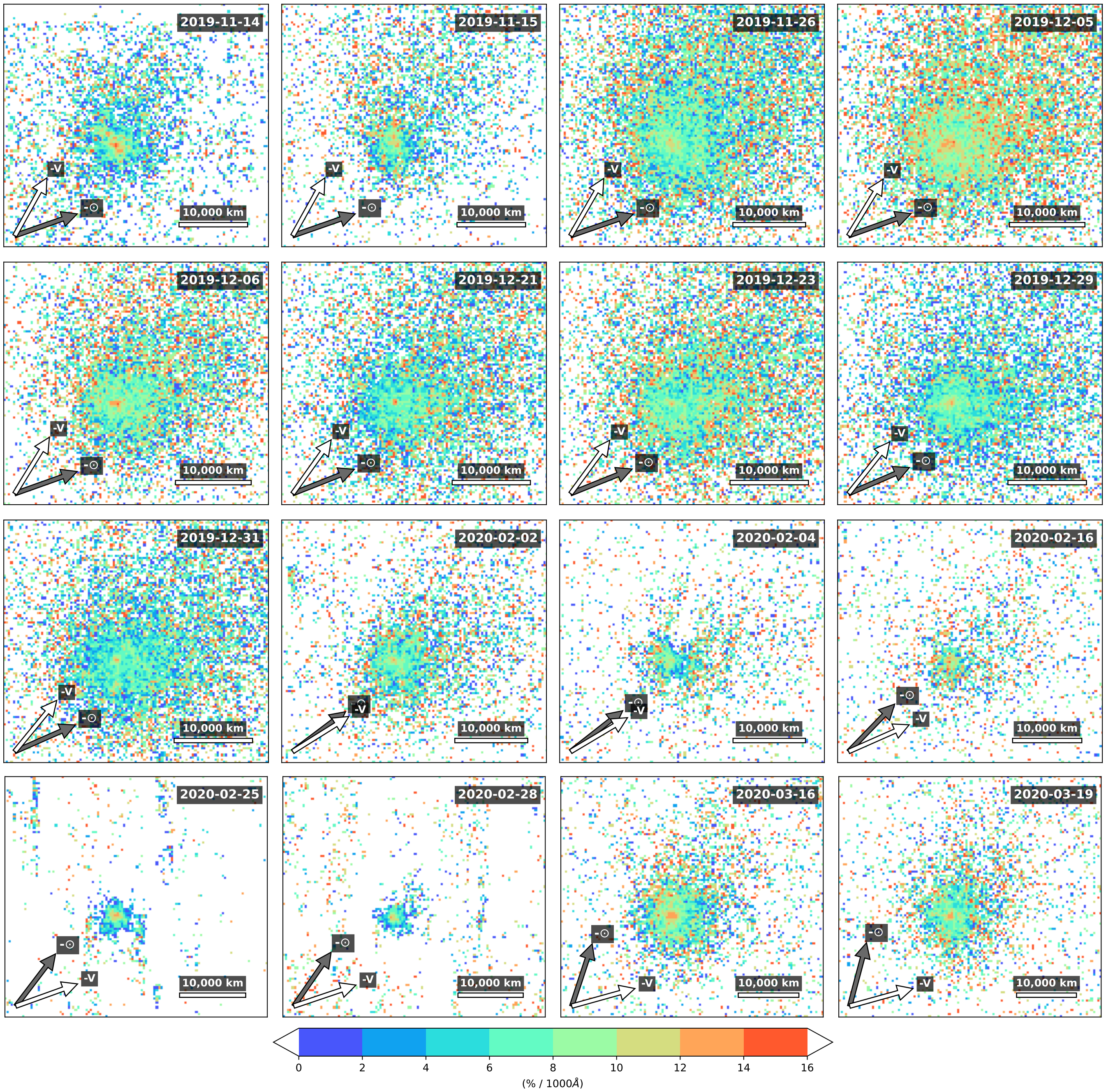

Figure 4. Distribution of normalized solar reflectance gradients for 2I/Borisov. The very inner coma has a steeper gradient, between 10% and 14% in comparison to the outer coma, within 4% and 10%. The extreme values in white represent the sky and background star streaks. North is up, east is to the left, and the antisolar (-⊙) and negative velocity ($-\boldsymbol{V}$) directions are shown with the respective arrows.

from their inner to outer annuli for 2019 December 02. While most of the change of color we observe with 2I is close to the optocentre and within E. Mazzotta Epifani et al. (2021)'s inner-most annulus radius of 2 x 10^3 km (one fifth of the scale bar in Figure 4), we also see the trend of decreasing spectral slope out to 1.3×10^4 km.

As mentioned above, we do not see a substantial change in dust color with heliocentric distance or time. There is only a slight downward trend in the dust color over time (highlighted further in Section 5.1). This is in contrast with previous reports from V. V. Busarev et al. (2021), who found that the reflectance varied over time periods of a few days. They attributed that change to an increasing contamination from gas emission in their filters, which is not our case since we selected bands containing only continuum signal for our color analysis.

4.2. Dust Maps

Figure 6 presents the original dust maps, while Figure 7 shows the same maps after image enhancement. The nights have varying levels of noise depending on the number of exposures coadded and the observing conditions. Several features can be distinguished in the dust maps. On November 14, 15, 26, and December 5 and 6, there is a clear elongation in Figure 6 toward the northwest, corresponding to a broad feature in the enhanced maps of Figure 7. Such asymmetry is

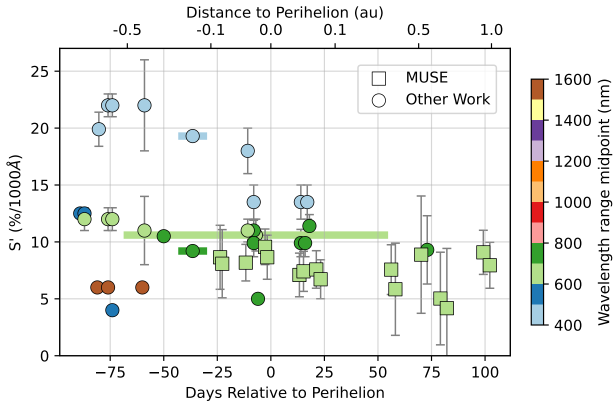

Figure 5. Dust color, S', of 2I from both MUSE (squares; 5000 km diameter aperture) and reported literature values (circles) relative to perihelion. Any reported value calculated from multiple observations has a horizontal line behind it spanning the range of dates. This data is also listed in Appendix B, along with the wavelength range over which S' was measured.

also seen in Y. Kim et al. (2020). In Figure 7, we see a jetlike feature toward the west, curving toward the northwest at larger nucleocentric distances as indicated by the dashed lines. This becomes distinctly visible for all dates from November 26 onward, though it does not appear to extend as far from the nucleus when 2I is fainter in the 2020 observations. In the December observations, which have the best signal, we can see the curve begins in the antisolar direction (west) and curves toward the negative velocity direction (northwest). The jet stays within approximately 20 degrees of the antisolar direction for the rest of the observations. The post-`starkiller` data permit observations with dense stellar crowding in February to be assessed. We do not see any significant evolution of the dust morphology between the end of November 2019 and March 2020, i.e., through perihelion. E. Mazzotta Epifani et al. (2021), B. T. Bolin & C. M. Lisse (2020), and F. Manzini et al. (2020) all report observations of 2I in 2019 December and 2020 January (only 2020 January for F. Manzini et al. 2020). Their observations are consistent with what we see in the MUSE data; they report a jetlike feature toward the west. Since some of the observations are from HST —with a much better spatial resolution than our MUSE data and processed with different techniques—it would seem to confirm that the feature we observe toward the northwest is real and not an artifact of the enhancement technique we applied. These authors also report a smaller and fainter jetlike feature toward the east/northeast in the HST data; we do not see this in our data.

As we only obtained one epoch of imaging per night, we cannot assess whether the dust feature to the west/northwest changed on short timescales that might correspond to the rotation of the nucleus. However, the lack of substructure often associated with rotational variation (like a corkscrew or pinwheel; T. L. Farnham 2009) suggests that rotational variation would have been difficult to identify even if the data existed. Such structures are typically identified in gas images rather than dust. Even in comets with such structures evident in their gas, the dust jets tend to show little to no variation (e.g., 103P/Hartley 2 M. M. Knight & D. G. Schleicher 2013; B. E. A. Mueller et al. 2013). Identification of coma structures was further hindered by the large geocentric distance, which was always >1.9 au; previous detections have generally been made when a comet was within 0.5 au of Earth.

The feature's appearance was very similar from night to night and only gradually evolved over the course of the apparition. Thus, we postulate that the changing appearance was likely due to the changing viewing geometry. The relatively constant direction of the feature toward the west may indicate a preferential direction for ejection of dust, perhaps due to the pole orientation and direction of rotation, but modeling to investigate this is beyond the scope of this paper.

Our dust maps (Figures 6 and 7) do not resolve the March splitting event, but are otherwise consistent with the HST observations by D. Jewitt et al. (2020) in the broadband F350LP filter, which saw general antisolar elongation in 2I's coma on 2020 March 23. Some split comets have exhibited a double "wing" structure orthogonal to the comet–Sun line (see review by H. Boehnhardt 2004), which T. L. Farnham (2009) showed was a product of the image enhancement choice. For the azimuthal median subtraction we employed, this would manifest as two lobes centered on the comet–Sun line. No such structures were seen, but given the low SNR by this time, their absence is not necessarily significant.

4.3. Gas Maps

The spatial distribution of C_2, NH_2, and CN is presented in Figure 8 for observations on 2019 December 5 and 6. This figure reveals a very similar morphology for C_2, NH_2, and CN. Their distribution is roughly symmetrical around the optocentre, with a hint of extension toward the northwest for CN. The maps for all dates are in Appendix C. The comet is only detected in our C_2 and NH_2 maps in 2019 (with the exception of NH_2 in one post-outburst epoch), while CN is detected through 2019–2020. Taking into account the relatively low SNR of the maps, we do not see any significant changes in the gas morphology over the apparition. There appears to be a feature of CN emission to the northwest within 2000 km of the optocentre of 2I on 2020 March 19; however, it was only visible in one of the three contributing data cubes. We conclude it is contamination from background stars in the same position that was not suppressed during the median coadding of exposures. The SNR was insufficient to reveal any morphological features in the gas maps under image enhancement.

4.4. Production Rates

Our C_2, NH_2, and CN production rates are provided in Table 4 and shown in Figure 9, together with the values in the literature. The production rates display different trends with time and heliocentric distances. We measured a slight decrease in the CN production rate between November 14/15 and December 23, when 2I was at 2.08 au from the Sun pre-perihelion and 2.03 au post-perihelion, respectively. After that date, we saw a relatively constant CN production rate with heliocentric distance. The CN production rate increased for our last two measurements on March 16 and 19. Unlike CN, both the NH_2 and the C_2 production rates decreased from the start of our observations until February 28 ($r_h = 2.7$ au), but showed an increase similar to CN on March 16 and 19. We discuss rate changes relative to 2I's splitting event in Section 5.1.

Other authors have previously reported gas production rates for 2I at a similar time to some of our observations. As illustrated in Figure 9, our measurements are consistent with the production rates of C_2 and CN in H. W. Lin et al. (2020).

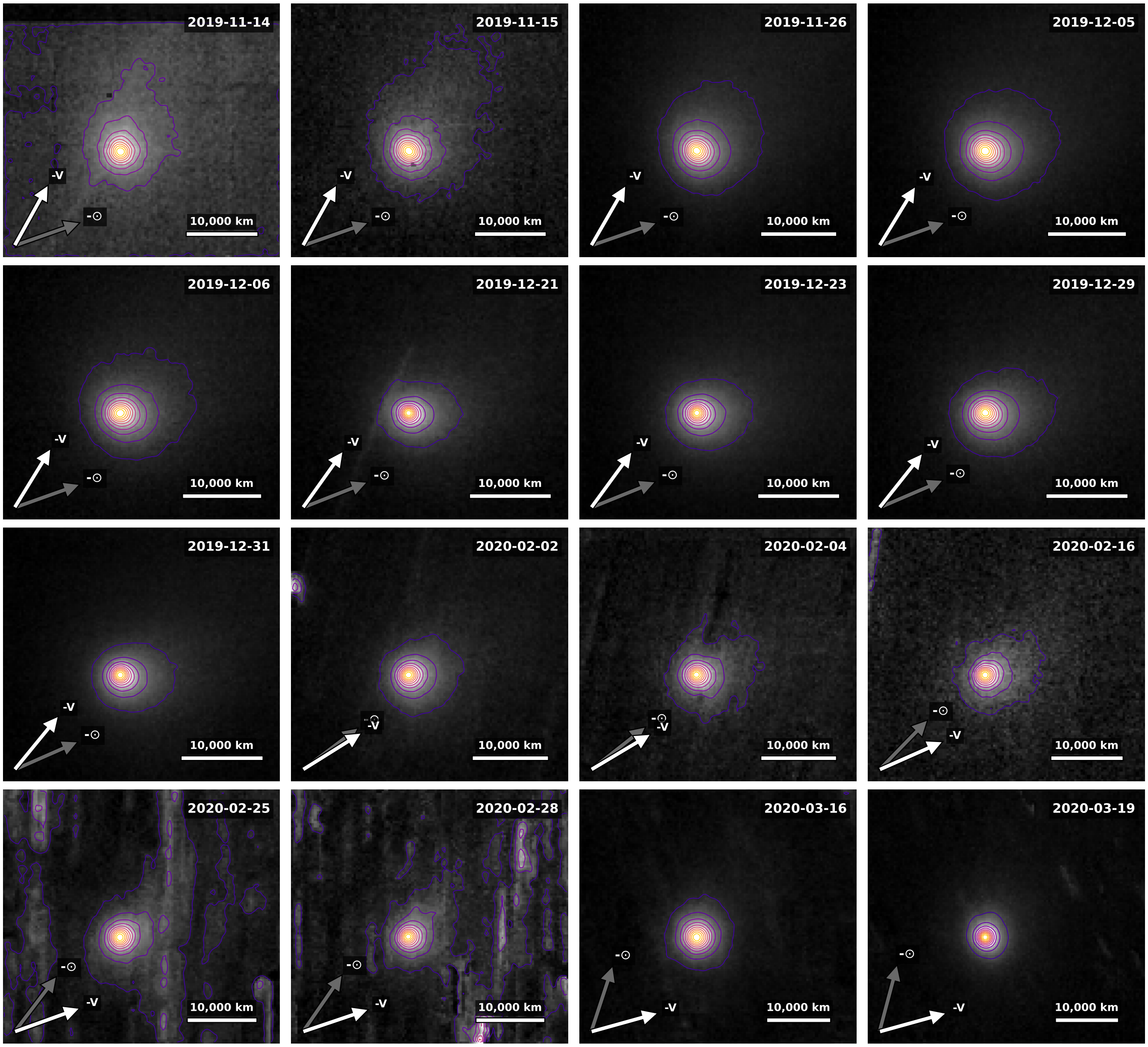

Figure 6. Dust emission maps spanning 2019 November 14 until 2020 March 19 displayed with a linear stretch and the same orientation as Figure 4. Streak effects are due to background stars (minimized by the application of `starkiller`). The contours (also fitted to the background stars and the edge of the FOV) at 9% intervals show the elongation of the dust in the coma in relation to the antisolar (-⊙) and negative velocity ($-\boldsymbol{V}$) directions.

They are significantly lower than those reported by K. Aravind et al. (2021) for 2019 December 22 and 2019 November 30; the discrepancy could be due to the difference in aperture used to extract the spectrum or the velocity used[21] in the Haser model. If we use the same velocity, our measurements are mostly in agreement with those from K. Aravind et al. (2021) at the end of November. We also note that the CN band we used is different from the CN band used in most other studies, which could contribute to discrepancies. Our rates of NH_2 production are several times higher than those of G. P. Prodan et al. (2024) for a similar date. The reason for this discrepancy is difficult to identify, but could be attributed to the different fluorescence bands ((0,10,0) versus (0,8,0)), or a difference in aperture used. The fluorescence efficiencies used might also play a role. We, for example, note that there is a factor 2 between the fluorescence efficiencies from S. Tegler & S. Wyckoff (1989) and C. Arpigny (1994) for the (0,10,0) band. In this work, we used a relatively small aperture of 5000 km to avoid contamination by stars as 2I was crossing the galactic plane. If the radial profile of the species does not match the Haser profile well (which we cannot verify due to low SNR), the aperture size will have a significant impact on the production rates derived.

The production rates presented here are slightly different from those reported in M. T. Bannister et al. (2020) using the same data, but consistent within the uncertainty. This could be attributed to a combination of factors. First, the aperture used is different: 10″ in M. T. Bannister et al. (2020), corresponding to about 15,000 to 17,000 km versus 5000 km here. The largest difference arises for C_2, which is not surprising, as it has long been known that C_2 profiles are often observed to be flatter at

[21] K. Aravind et al. (2021) use 1 km s^{-1} (K. Aravind 2022, personal communication) while we use 0.5 km s^{-1}.

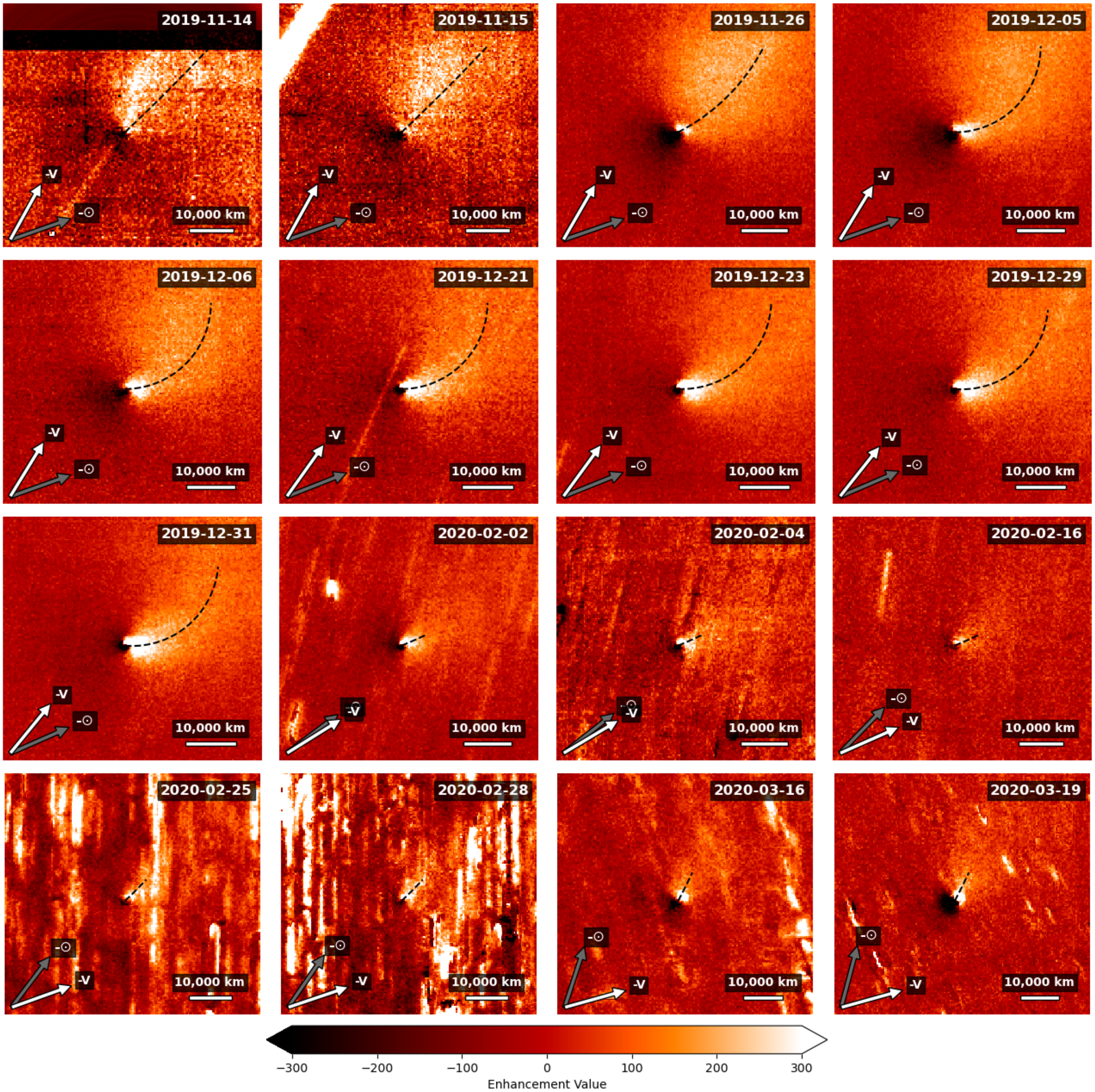

Figure 7. Dust maps from Figure 6, enhanced by subtraction of azimuthal median with the same orientation as Figure 4. Dashed lines trace the consistent jetlike feature toward the northwest, shown with higher enhancement values. The length of the dashed annotations reflects the radial extent of the jet that is visible in these observations, which decreases as 2I receded from perihelion. Streak effects are due to background stars (minimized by the application of `starkiller`). The dark bands on 2019 November 14 are the edge of the image.

low heliocentric distances compared to the Haser profiles. This means that if a smaller aperture is used, it can lead to lower production rates. L. Ferellec et al. (2024) have demonstrated that this can lead to differences in derived production rates of up to a factor of 2. The telluric absorption was also dealt with differently. In M. T. Bannister et al. (2020), we used the telluric correction from the MUSE pipeline, while here we performed an actual fit of the telluric features using the Molecfit software, leading to a better correction in the redder part of the spectrum where the CN emission is located. This is consistent with the largest differences being observed for the CN. We provide an update to Figure 5 of M. T. Bannister et al. (2020), placing 2I's NH_2 production within the context of solar system comets (Figure 10).

5. Discussion

We computed abundance ratios between the different species we observed; these are shown in Figure 9. We measured a $Q(C_2)/Q(CN)$ ratio between 0.1 and 0.3. This confirms that if 2I were a solar system comet, it would be in the category of carbon-chain depleted comets, which were

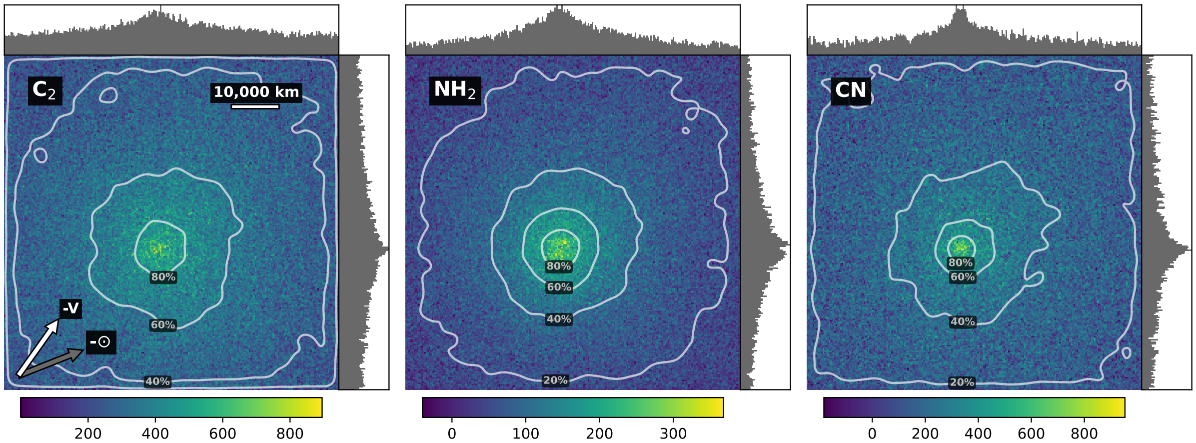

Figure 8. Relative spatial distribution of the C_2, NH_2, and CN gas using maps coadded from 2019 December 5 and 6 (7 × 600 s exposures). The histogram above/beside each map shows the sum of flux from a horizontal/vertical strip 10 pixels wide (a projected distance of 2900 km) through the comet center. All images are displayed with a linear stretch over a zmax scale and the same orientation as Figure 4. The contours are 20% flux intervals of the gas maps after smoothing by a 5 standard deviation Gaussian convolution. The 20% flux line of C_2 is not labeled to avoid crowding. All images are 48″ (~70,000 km at the distance of 2I) wide with a scale length of 1″ = 1460 km.

defined by M. F. A'Hearn et al. (1995) as $Q(C_2)/Q(CN) < 0.66$, as opposed to a "typical" comet measuring 0.7–2.0. The carbon-chain depleted comets are more abundant within the Jupiter Family Comet and Short Period Comet populations (see M. F. A'Hearn et al. (1995); their Figure 16). The comets belonging to these dynamical classes are formed within the Kuiper Belt region, further from the Sun than the Uranus–Neptune region where Oort cloud comets formed. The observed carbon-chain depletion is therefore consistent with the high CO measurements of M. A. Cordiner et al. (2020) and the notion that 2I formed beyond the CO ice line of its host star, with similar conditions for the creation of carbon-chain molecules that exist within the Kuiper Belt. Additionally, we saw a tentative decreasing trend in the $Q(C_2)/Q(CN)$ with heliocentric distance in our post-perihelion data. This would also be consistent with the $Q(C_2)$ upper limits reported by A. Fitzsimmons et al. (2019), H. W. Lin et al. (2020), and J. de León et al. (2020) for observations in September and October 2019, some of which result in a $Q(C_2)/Q(CN)$ lower than what we measure in November 2019.

Changes in the $Q(C_2)/Q(CN)$ ratios during passage in the inner solar system have been seen for some solar system comets. In their study of a group of comets, L. E. Langland-Shula & G. H. Smith (2011) found a decrease in the ratio with the heliocentric distance. This was also reported by C. Opitom et al. (2015) for comet C/2016 F6 (Lemmon). The origin of the decrease is still unclear, but it has been postulated that it could be related to the model parameters (e.g., scale lengths) used in the Haser model. However, other large studies of comet composition have not shown that this trend exists systematically among comets (A. L. Cochran et al. 2012; M. F. A'Hearn et al. 1995; U. Fink 2009). Thus, the trend we observe for the $Q(C_2)/Q(CN)$ ratio of 2I/Borisov is rare, but not unprecedented among solar system comets.

We also measured a $Q(NH_2)/Q(CN)$ ratio in the range 0.7–2.1, with an average of 1.7. This value is on the high side compared to U. Fink (2009), A. L. Cochran et al. (2012), and L. E. Langland-Shula & G. H. Smith (2011)'s samples of solar system comets: see Figure 10. This is consistent with our initial assessment in M. T. Bannister et al. (2020): 2I is relatively rich in NH_2 compared to most solar system comets.

Over the observing period targeted in this work, we saw a decrease in NH_2 and C_2 abundances that was sharper than that for CN. D. Bodewits et al. (2020) report a similar effect for H_2O and CO over the same time interval, with the H_2O abundances decreasing while CO remains almost constant. This behavior could be indicative of NH_2 and C_2 being released from a similar source region as H_2O, while CN is more correlated with the CO, or that a region with higher CN and CO abundances was illuminated post-perihelion. However, given the uncertainties in the abundances due to the faintness of the target, it is impossible to investigate this further.

Morphological features, such as jetlike features, in a comet's coma have been attributed in the past to active areas on the nucleus of comets. Changes in the shape or number of visible features have thus been hypothesized to be linked with changes in the illuminated areas on the nucleus. Previous studies focusing on measuring gas production rates in the coma of 2I have shown significant changes in relative abundances in its coma between pre- and post-perihelion observations, which they attributed to a seasonal effect (Z. Xing et al. 2020; K. Aravind et al. 2021). Our morphological observations of the dust coma of 2I, however, did not reveal any evidence of a seasonal effect.

The multispecies production and uniform activity of 2I indicate a volatile-rich object. This is in contrast to 1I/'Oumuamua, which appeared devolatilised with a reddened surface (e.g., M. T. Bannister et al. 2017; A. Fitzsimmons et al. 2018). We confirm that 2I/Borisov therefore formed beyond ice lines, in the outer part of its system's disk. Our data do not further tie down a disk formation location or constrain the M dwarf origin suggested by M. A. Cordiner et al. (2020) and D. Bodewits et al. (2020).

The presence of volatiles indicates that 2I had minimal processing prior to leaving its parent system. This is supported by the CO and polarization measurements in other data (D. Bodewits et al. 2020; M. A. Cordiner et al. 2020; S. Bagnulo et al. 2021; P. Halder & S. Sengupta 2023), and the dynamics of ISOs in the Galaxy (J. C. Forbes et al. 2025), which predict that ISOs have exceptionally low probabilities for any close stellar encounters after unbinding, i.e., the default

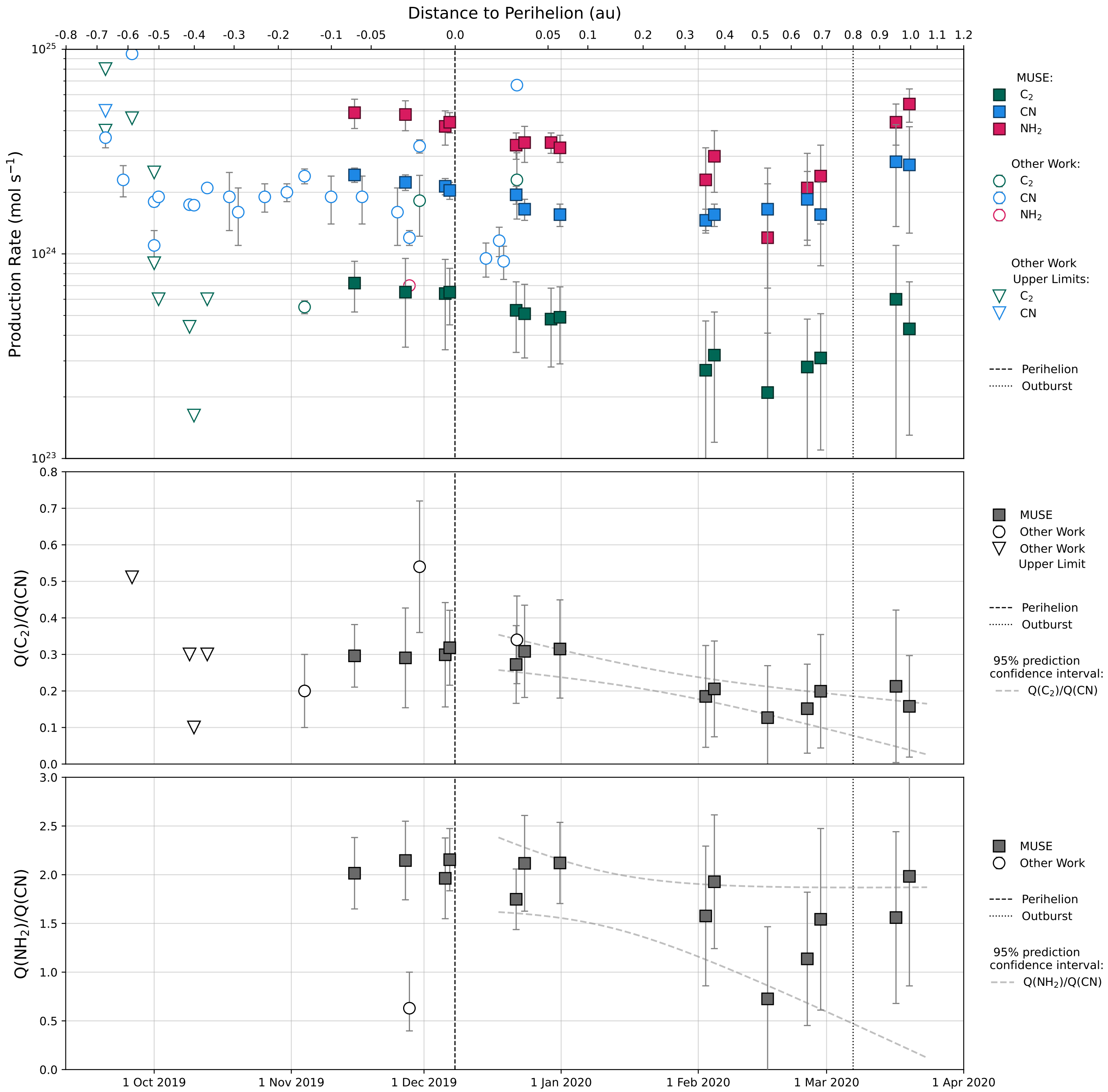

Figure 9. C_2, NH_2, CN production rates (upper figure), $Q(C_2)/Q(CN)$ ratio (middle figure), and $Q(NH_2)/Q(CN)$ ratio (lower figure) for 2I from 20 September 2019 to 19 March 2020. Our measurements are shown next to other sources: A. Fitzsimmons et al. (2019), J. de León et al. (2019), T. Kareta et al. (2020), C. Opitom et al. (2019b), H. W. Lin et al. (2020), M. T. Bannister et al. (2020), K. Aravind et al. (2021), M. A. Cordiner et al. (2020), G. P. Prodan et al. (2024). Note that the measurements of $Q(C_2)/Q(CN) < 1$ on 2019 September 20 (A. Fitzsimmons et al. 2019) and $Q(C_2)/Q(CN) < 2.3$ on 2019 October 1 (T. Kareta et al. 2020) are omitted. The 95% confidence interval windows for the production rate ratios are shown as light gray dashed lines and are predicted for post-outburst dates by extrapolating the pre-outburst values.

assumption should be that they are not thermally heated during galactic travel.

Looking to our own solar system as an exemplar, the thermal processing of a comet is intrinsically linked to its dynamical history (A. Gkotsinas et al. 2024). Bodies that migrated to an Oort cloudlike orbit are more likely to be pristine in nature, while bodies ejected from the solar system during giant planet migration are statistically more processed. This could indicate that 2I's ejection mechanism was more akin to gently drifting from an Oort cloud, as opposed to early planetary scattering—despite ongoing unbinding of Oort cloud objects from systems only contributing $\gtrsim$10% of the ISO population (S. Portegies Zwart 2021). For a summary of ISO ejection mechanisms, see Section 4 of A. Fitzsimmons et al. (2024).

Studying more active ISOs will enable us to understand whether all ISOs are like 2I or if they have a range of activity, shedding light on the ejection mechanisms of ISOs in the Milky Way. M. J. Hopkins et al. (2025) find that, based on its kinematics, 2I could originate from a star of a broad range of

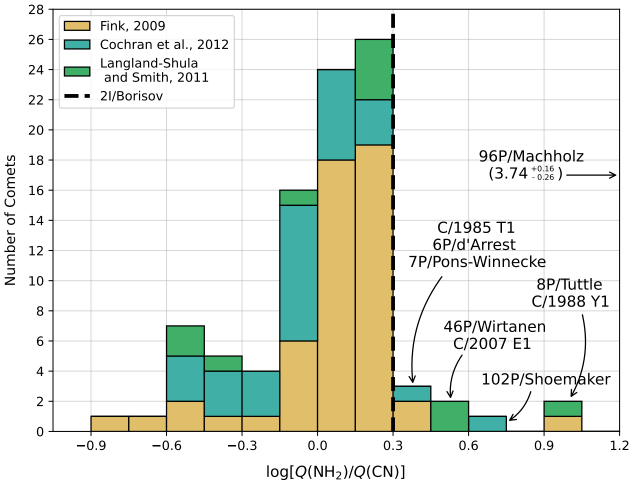

Figure 10. Ratio of NH_2 to CN production for solar system comets in comparison to the average of 2I/Borisov about perihelion (dashed line). Several other comets from the collections of U. Fink (2009), A. L. Cochran et al. (2012), and L. E. Langland-Shula & G. H. Smith (2011) have shown NH_2 to CN ratios higher than 2I/Borisov; these are individually labeled. Note that the histogram bars per collection are stacked.

ages, all across the Galaxy; our findings remain consistent with this argument.

5.1. Post-splitting Behavior

A brightness increase indicating an outburst of 2I was detected around March 4–9 in ground-based observations (M. Drahus et al. 2020). Spatially separated fragments, and associated brightening from $H = 14.45$ to $H = 14.19$, were detected in HST observations made using the broadband F350LP filter (D. Jewitt et al. 2020). Our observations and those of D. Jewitt et al. (2020) both bracket the split. Fortuitously, both datasets were acquired by the facilities' respective queues with a very similar observing cadence, differing by only 1–3 days (we indicate the respective cadences in Figure 11). Our interpretations are strengthened by correlating our data to the photometry of D. Jewitt et al. (2020), who directly observed the nucleus splitting. This fragmentation event thus provided a unique opportunity to probe the composition of the interior of 2I's nucleus.

On fragmenting, 2I produced much more NH_2. The NH_2 gas production rate showed a statistically significant (>95% confidence interval) increase above the pre-outburst trends (Figure 11). The post-split C_2 and CN production rates also showed an increase, though the uncertainties are much larger. There is a large scatter in the post-perihelion $Q(NH_2)/Q(CN)$ ratios, while $Q(C_2)/Q(CN)$ decreased post-perihelion consistently. Neither species ratios, however, show a statistical change from the post-perihelion trends after the outburst, so we cannot discern any change in ice composition of 2I due to the outburst. At the SNR of our measurements, we do not see any change in the gas morphology that could be linked to the outburst. 2I potentially experienced a slight increase in the slope of the dust color (i.e., reddening) after the reported outburst (Figure 11). There was a trend of decreasing S' as 2I receded from perihelion, upon which we calculated the predictive interval by extrapolating the pre-outburst values (see Section 3.2.1). The post-outburst S' lie outside this predictive interval, although they only rise to levels comparable to those observed near perihelion and are within the

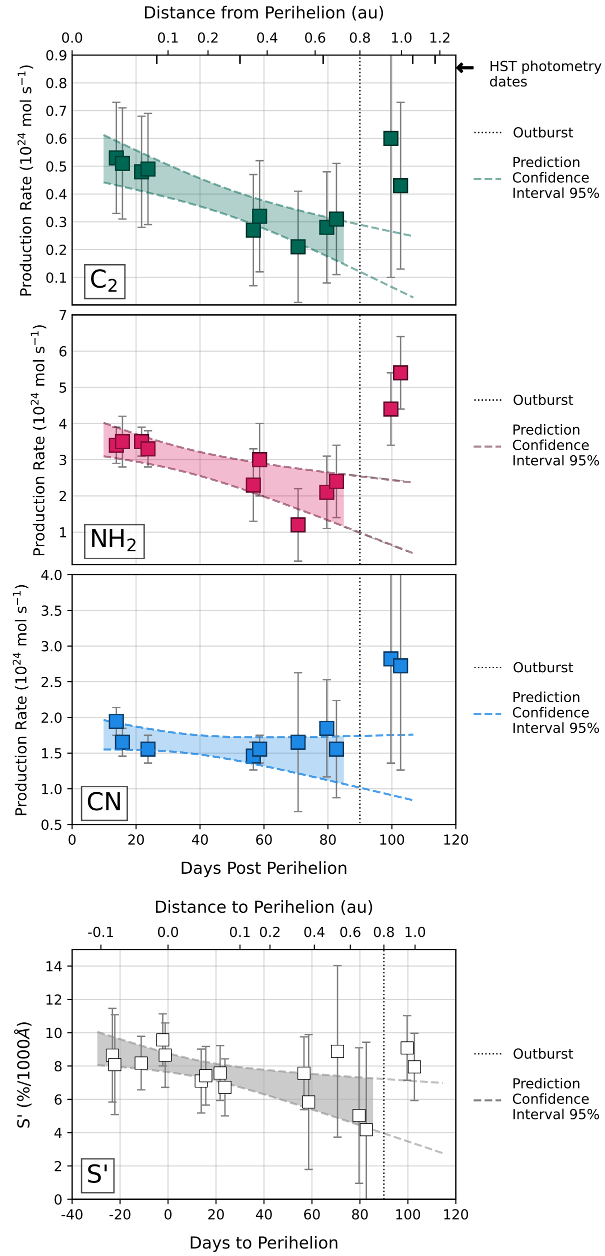

Figure 11. MUSE-observed C_2, NH_2, and CN production rates and the dust color S' measurements. The 95% confidence interval windows for the production rates are predicted on the post-perihelion, pre-outburst values, while the interval for S' is predicted on all pre-outburst values. NH_2 showed a clear increase in production after the outburst. C_2 and CN also increased, but the uncertainties fall within the expected pre-outburst trend. S' also shows a minimal increase, i.e., 2I's color reddened. The dates of HST photometry from D. Jewitt et al. (2020) are indicated by tick marks along the top axis. Our post-outburst observations overlap with two of these dates, where D. Jewitt et al. (2020) measured 2I as significantly brighter than before the outburst.

uncertainties of the noisy February data. We infer that this deviation in 2I's dust color from the expected trend after the outburst is potentially linked to an exposure of larger particles from the freshly exposed surface, and indicative of the top layer of 2I's nucleus being slightly depleted in volatiles since perihelion (around 90 days). The dust morphology of 2I (Figures 6 and 7) does not appear to change with the outburst.

Our observations of 2I's composition do not show any conclusive heterogeneity of the nucleus ice composition. Any changes we see would need to be significantly beyond measurement uncertainties to be certain that our assumptions, for example, the gas profile for the Haser model, are well-suited to analyzing 2I both before and after the outburst. A homogeneous nucleus would be similar to the comet 73P/Schwassmann–Wachmann 3, which displayed a constant composition of ices after its fragmentation (N. Dello Russo et al. 2007; D. G. Schleicher & A. N. Bair 2011). If 2I did experience some processing, either at its host star or during its interstellar passage, it must have been minimal.

5.2. Expectations for Observations of Future ISOs

Upcoming sky surveys such as the Vera Rubin Observatory's Legacy Survey of Space and Time (LSST) and NEOSurveyor are anticipated to provide a substantial sample of additional ISOs to characterize. Choices will have to be made about target prioritization. 2I was characterizable with MUSE for a time consistent with the predictions of R. C. Dorsey et al. (2025; see their Figure 16). We note that LSST would discover a 2I-equivalent object at a greater heliocentric distance than 2I's 3 au, due to the survey's depth being nearly 100 times greater than 2I's discovery brightness, which would increase the characterization window from what MUSE achieved here. However, future ISOs are likely to be found by LSST equally both before and after perihelion (R. C. Dorsey et al. 2025), so not all ISOs will be able to have campaigns throughout perihelion like the one we present here. In particular, the post-perihelion discoveries only have a median 73 day window for spectroscopic characterization. As the LSST sample is predicted to comprise of order tens of ISOs, multiepoch campaigns on ISOs will continue to be needed for comparative characterization. As demonstrated in this work, because of the IFU nature of MUSE, we were able to retrieve a lot of information while 2I was crossing the Galactic plane, which would not have been possible if we had used a regular long-slit spectrograph. As shown in M. J. Hopkins et al. (2025), future ISOs are likely to spend substantial time on the Galactic plane, which is also the case for the recently announced[22] third ISO, 3I/ATLAS. For future rare extended objects that are only visible for a limited time window, using the MUSE instrument would then be an excellent option.

6. Conclusion

We used observations with the MUSE IFU to constrain the morphology and composition of 2I/Borisov for an extensive amount of its observing passage. This forms the longest large-aperture dataset yet acquired for the perihelion passage of an ISO, and the only dataset on 2I's composition sampled throughout its entire visible window. As the post-perihelion data fell on the Galactic plane, we developed the star-subtraction package `starkiller` (R. Ridden-Harper et al. 2025); this significantly improved the usefulness of the data acquired during 2I's recession for assessing the dust in its comae. From this analysis of dust color, dust, C_2, NH_2, and CN gas species morphology, and the gas species production rates, we are able to see that:

1. 2I retains volatiles and is uniformly active, indicating minimal processing before it left its parent system.
2. Considered relative to solar system comets, 2I is carbon-depleted, but fairly NH_2-rich.
3. On splitting, 2I revealed material that led to a substantial increase in NH_2 production.

2I displays both similarities and differences from comets in the solar system. The common aspects of 2I/Borisov with comets in our own system suggest planetesimal formation processes happen in similar ways across the Galaxy, in both space and time. ISOs thus hold both the promise of unveiling the subtleties of protoplanetary disk variation and affirm the Copernican principle as applied to planetesimal formation across the cosmos.

Acknowledgments

Based on observations collected at the European Southern Observatory under ESO programs 103.2033.001–003 and 105.2086.002. We thank the ESO staff, particularly Henri Boffin, Diego Parraguez, Edmund Christian Herenz, Fuyan Bian, and Israel Blanchard, for their help in the acquisition of these observations.

We would like to thank John Forbes for his helpful advice on statistics.

M.T.B. appreciates support from the Rutherford Discovery Fellowships from the New Zealand Government funding, administered by the Royal Society Te Apārangi.

D.Z.S. is supported by an NSF Astronomy and Astrophysics Postdoctoral Fellowship under award AST-2303553. This research award is partially funded by a generous gift of Charles Simonyi to the NSF Division of Astronomical Sciences. The award is made in recognition of significant contributions to the Rubin Observatory's Legacy Survey of Space and Time.

S.E.D. acknowledges the support of an Australian Government Research Training Program Scholarship.

This research made use of the Canadian Advanced Network for Astronomy Research (CANFAR) and the facilities of the Canadian Astronomy Data Center operated by the National Research Council of Canada with the support of the Canadian Space Agency. This research has made use of data and/or services provided by the International Astronomical Union's Minor Planet Center.

The views expressed in this article are those of the authors and do not reflect the official policy or position of the U.S. Naval Academy, Department of the Navy, the Department of Defense, or the U.S. Government.

Facility: VLT (MUSE).

Software: `astroplan` (B. M. Morris et al. 2018), `astroquery` (A. Ginsburg et al. 2019), Astropy (Astropy Collaboration et al. 2022), `jplephem` (B. C. Rhodes 2011), Matplotlib (J. D. Hunter 2007), MUSE Python Data Analysis Framework (MPDAF) R. Bacon et al. (2016), NumPy (C. R. Harris et al. 2020), pandas (W. McKinney 2010; pandas development team T. 2020), Photutils (L. Bradley et al. 2023), SciPy (P. Virtanen et al. 2020), `starkiller` (R. Ridden-Harper et al. 2025), statsmodels (S. Seabold & J. Perktold 2010).

Appendix A
Observation Information

Appendix A provides the observational metadata for 2I. Table 5 summarises the observing geometry and identifies which observations were included in, or excluded from, specific analyses. Table 6 lists the calibration stars observed at each epoch and used for flux calibration.

[22] 2025 July 2: https://minorplanetcenter.net/mpec/K25/K25N12.html.

Table 5
VLT/MUSE Observations of 2I/Borisov, with Geometric Relationships between 2I, Earth, and the Sun

Observation Date (UTC)	Altitude[1] (deg)	Airmass[2]	DIMM Seeing[3] (arcsec)	r_h [4] (au)	Δ [5] (au)	Elongation[6] (deg)	α [7] (deg)	$\theta_{-\odot}$ [8] (deg)	θ_{-V} [9] (deg)	l[10] (km)
2019 Nov 14 08:03:10	28.7	2.17	0.8	2.08	2.23	68.25	26.26	289.29	330.98	1617
2019 Nov 14 08:19:45	32.4	1.95	0.8	2.08	2.23	68.25	26.26	289.29	330.98	1617
2019 Nov 14 08:31:36[a]	35.0	1.82	0.72	2.08	2.23	68.25	26.26	289.29	330.98	1617
2019 Nov 14 08:48:23[a]	38.6	1.67	0.72	2.08	2.23	68.26	26.26	289.29	330.98	1617
2019 Nov 15 08:02:02	29.3	2.13	0.87	2.07	2.22	68.60	26.40	289.25	330.94	1608
2019 Nov 15 08:18:33	32.9	1.92	0.68	2.07	2.22	68.61	26.40	289.25	330.93	1608
2019 Nov 15 08:30:28[a]	35.5	1.79	0.76	2.07	2.22	68.61	26.40	289.25	330.93	1608
2019 Nov 15 08:53:20[a]	40.5	1.60	0.57	2.07	2.22	68.61	26.40	289.25	330.93	1607
2019 Nov 26 07:17:24	28.0	2.16	0.43	2.02	2.09	72.41	27.69	289.11	330.02	1517
2019 Nov 26 07:34:33	31.9	1.93	0.74	2.02	2.09	72.42	27.69	289.11	330.02	1517
2019 Nov 26 07:46:28	34.6	1.79	0.8	2.02	2.09	72.42	27.69	289.11	330.02	1517
2019 Nov 26 08:03:33	38.5	1.64	0.74	2.02	2.09	72.43	27.70	289.11	330.02	1516
2019 Dec 5 07:09:26	33.2	1.82	0.93	2.01	2.02	75.40	28.36	289.50	328.65	1462
2019 Dec 5 07:26:38	37.2	1.66	1.34	2.01	2.02	75.40	28.36	289.50	328.65	1462
2019 Dec 5 07:38:31	39.9	1.57	1.17	2.01	2.02	75.40	28.36	289.50	328.65	1462
2019 Dec 5 07:55:01	43.6	1.46	1.21	2.01	2.02	75.41	28.36	289.50	328.64	1461
2019 Dec 6 07:37:32	40.4	1.55	1.04	2.01	2.01	75.73	28.42	289.57	328.45	1457
2019 Dec 6 07:53:57	44.1	1.45	1.61	2.01	2.01	75.73	28.42	289.57	328.45	1457
2019 Dec 6 08:05:52	46.9	1.38	1.35	2.01	2.01	75.73	28.42	289.57	328.45	1456
2019 Dec 6 08:25:06[a]	51.2	1.30	1.47	2.01	2.01	75.74	28.42	289.57	328.45	1456
2019 Dec 21 07:56:19	54.8	1.21	0.49	2.03	1.94	80.39	28.60	291.52	324.50	1410
2019 Dec 21 08:13:29	58.6	1.16	0.57	2.03	1.94	80.39	28.60	291.52	324.49	1410
2019 Dec 21 08:25:25[a]	61.2	1.13	0.65	2.03	1.94	80.40	28.60	291.52	324.49	1409
2019 Dec 21 08:42:26[a]	64.9	1.10	0.51	2.03	1.94	80.40	28.60	291.53	324.49	1409
2019 Dec 23 05:50:43	28.8	1.98	0.39	2.03	1.94	80.96	28.55	291.89	323.84	1407
2019 Dec 23 06:07:20	32.3	1.80	0.28	2.03	1.94	80.97	28.55	291.89	323.83	1407
2019 Dec 23 06:19:16	34.9	1.69	0.44	2.03	1.94	80.97	28.55	291.89	323.83	1407
2019 Dec 23 06:42:59	40.0	1.52	0.32	2.03	1.94	80.97	28.55	291.89	323.82	1407
2019 Dec 29 05:18:41	26.2	2.12	0.66	2.06	1.94	82.74	28.30	293.22	321.54	1405
2019 Dec 29 05:38:15	30.2	1.89	0.71	2.06	1.94	82.74	28.29	293.23	321.53	1405
2019 Dec 29 05:50:13	32.6	1.77	0.6	2.06	1.94	82.74	28.29	293.23	321.53	1405
2019 Dec 29 06:09:06	36.5	1.62	0.48	2.06	1.94	82.75	28.29	293.23	321.52	1405
2019 Dec 31 05:36:51	31.1	1.83	0.41	2.07	1.94	83.33	28.18	293.74	320.68	1406
2019 Dec 31 05:53:46	34.5	1.69	0.38	2.07	1.94	83.33	28.18	293.74	320.68	1406
2019 Dec 31 06:05:41	36.9	1.60	0.41	2.07	1.94	83.33	28.18	293.74	320.67	1406
2019 Dec 31 06:22:04	40.2	1.49	0.32	2.07	1.94	83.34	28.17	293.74	320.67	1406
2020 Feb 2 04:17:53	33.6	1.66	0.45	2.35	2.08	93.18	24.71	307.01	302.04	1512
2020 Feb 2 04:34:27	35.9	1.57	0.53	2.35	2.08	93.18	24.70	307.02	302.03	1512
2020 Feb 2 04:46:27	37.6	1.52	0.64	2.35	2.08	93.18	24.70	307.03	302.02	1512
2020 Feb 2 05:03:48	40.0	1.45	0.54	2.35	2.08	93.19	24.70	307.03	302.01	1512
2020 Feb 4 03:18:11[b]	26.2	2.01	0.55	2.38	2.10	93.81	24.44	308.12	300.82	1522
2020 Feb 4 03:34:48[b]	28.4	1.89	0.66	2.38	2.10	93.81	24.44	308.13	300.81	1522
2020 Feb 4 03:46:44	30.1	1.80	0.44	2.38	2.10	93.81	24.44	308.13	300.80	1522
2020 Feb 4 04:05:56[b]	32.7	1.69	0.45	2.38	2.10	93.82	24.44	308.14	300.80	1522
2020 Feb 16 04:07:13	36.9	1.53	0.6	2.53	2.20	97.83	22.77	315.86	293.87	1593
2020 Feb 16 04:24:06	38.8	1.47	0.79	2.53	2.20	97.84	22.77	315.87	293.87	1593
2020 Feb 16 04:35:59[c]	40.1	1.44	0.66	2.53	2.20	97.84	22.77	315.88	293.86	1594
2020 Feb 16 04:51:50	41.8	1.39	0.47	2.53	2.20	97.84	22.77	315.88	293.86	1594
2020 Feb 16 05:04:46	43.1	1.36	0.47	2.53	2.20	97.85	22.77	315.89	293.85	1594
2020 Feb 25 03:28:18	35.4	1.57	0.81	2.65	2.28	101.03	21.49	322.76	289.78	1653
2020 Feb 25 03:43:47	36.9	1.52	0.61	2.65	2.28	101.04	21.49	322.77	289.78	1653
2020 Feb 25 03:55:37	38.1	1.49	0.75	2.65	2.28	101.04	21.49	322.78	289.78	1653
2020 Feb 25 04:11:53	39.7	1.44	0.49	2.65	2.28	101.04	21.49	322.79	289.77	1653
2020 Feb 28 04:02:19[d]	39.4	1.45	0.72	2.70	2.31	102.14	21.06	325.32	288.69	1674
2020 Feb 28 04:20:27	41.0	1.41	0.65	2.70	2.31	102.15	21.05	325.33	288.69	1674
2020 Feb 28 04:32:18	42.0	1.38	0.6	2.70	2.31	102.15	21.05	325.34	288.69	1674
2020 Feb 28 04:48:45	43.3	1.35	1.22	2.70	2.31	102.15	21.05	325.35	288.68	1674
2020 Mar 16 04:41:49[b]	44.3	1.33	1.23	2.96	2.48	108.59	18.61	341.85	285.55	1801
2020 Mar 16 04:58:16	44.8	1.32	1.04	2.96	2.48	108.59	18.61	341.86	285.55	1801
2020 Mar 16 05:10:08	45.2	1.31	1.09	2.96	2.48	108.60	18.61	341.87	285.55	1801
2020 Mar 16 05:28:34[b]	45.5	1.30	1.11	2.96	2.48	108.60	18.61	341.88	285.55	1802
2020 Mar 19 05:23:42	45.3	1.31	0.61	3.00	2.52	109.74	18.19	345.14	285.50	1826
2020 Mar 19 05:46:49	45.4	1.30	0.32	3.00	2.52	109.75	18.18	345.16	285.50	1826

Table 5
(Continued)

Observation Date (UTC)	Altitude[1] (deg)	Airmass[2]	DIMM Seeing[3] (arcsec)	r_h [4] (au)	Δ [5] (au)	Elongation[6] (deg)	α [7] (deg)	$\theta_{-\odot}$ [8] (deg)	θ_{-V} [9] (deg)	l[10] (km)
2020 Mar 19 05:58:44[d]	45.4	1.30	0.36	3.00	2.52	109.75	18.18	345.17	285.50	1826
2020 Mar 19 06:14:45[b]	45.2	1.31	0.43	3.00	2.52	109.76	18.18	345.18	285.50	1826

Notes. (1) Starting altitude, (2) starting airmass, (3) FWHM seeing value at the beginning of the observation measured by the ASM-DIMM telescope, (4) heliocentric distance, (5) geocentric distance, (6) solar elongation angle, (7) solar phase angle, (8) position angle of the antisolar direction, (9) position angle of the negative velocity vector, (10) physical size of 1" projected to the distance of 2I in kilometers. Data obtained from the JPL Small-Body Database (https://ssd.jpl.nasa.gov/horizons/) using Astroplan and Astroquery.
[a] Discarded due to high twilight background.
[b] Omitted from production rates analysis due to 2I passing in front of a star.
[c] Discarded due to thin cloud conditions.
[d] Discarded due to 2I passing in front of a star.

Table 6
Spectrophotometric Standard Stars Imaged on Each Epoch and Used in Flux Calibrations

Observation Date	Object Name	Airmass
2019 Nov 14	LDS749B	1.2
2019 Nov 15	CPD-69 177	1.5
2019 Nov 26	CPD-69 177	1.4
2019 Dec 5	Feige110	1.2
2019 Dec 5	LTT3218	1.0
2019 Dec 6	LTT3218	1.0
2019 Dec 21	Feige110	1.3
2019 Dec 23	CPD-69 177	1.4
2019 Dec 23	GD71	2.8
2019 Dec 29	Feige110	1.8
2019 Dec 29	GD71 H13.90	1.4
2019 Dec 31	Feige110	1.4–1.5
2020 Feb 2	CPD-69 177	1.5
2020 Feb 4	GD71	1.3
2020 Feb 16	GD71	1.3
2020 Feb 16	HD49798	1.1
2020 Feb 25	GD71	1.3
2020 Feb 28	LTT3218	1.1
2020 Feb 28	EG274	1.1
2020 Mar 16	GD71	1.4
2020 Mar 16	EG274	1.0
2020 Mar 19	GD108	1.1

Appendix B
Data for Figures

Appendix B contains Table 7, which lists values of 2I's dust colour gathered from literature and used for comparison with the measurements in this work, as shown in Figure 5.

Table 7
Literature and MUSE-measured S'

S' (%/1000 Å)	Filters/Method	Range Used (nm)	Dates	Source
12.5	*g*' *r*'	475–630	2019 Sep 10	P. Guzik et al. (2020)
12.5	*g*' *r*'	475–630	2019 Sep 13	P. Guzik et al. (2020)
12 ± 1	spectroscopic	400–900	2019 Sep 13	J. de León et al. (2020)
6	spectroscopic	800–2400	2019 Sep 19	B. Yang et al. (2020)
19.9 ± 1.5	spectroscopic	390–600	2019 Sep 20	A. Fitzsimmons et al. (2019)
12 ± 1	spectroscopic	400–900	2019 Sep 24	J. de León et al. (2020)
22 ± 1	spectroscopic	390–600	2019 Sep 24	J. de León et al. (2020)
6	spectroscopic	800–2400	2019 Sep 24	B. Yang et al. (2020)
4	*B R*	440–650	2019 Sep 26	D. Jewitt & J. Luu (2019)
12 ± 1	spectroscopic	400–900	2019 Sep 26	J. de León et al. (2020)
22 ± 1	spectroscopic	390–600	2019 Sep 26	J. de León et al. (2020)
6	spectroscopic	800–2400	2019 Oct 09	B. Yang et al. (2020)
22 ± 4	spectroscopic	445–526	2019 Oct 10	T. Kareta et al. (2020)
11 ± 3	spectroscopic	526–713	2019 Oct 10	T. Kareta et al. (2020)
10.5	*R I*	647–797	2019 Oct 19	E. Mazzotta Epifani et al. (2021)
19.3	spectroscopic	390–600	2019 Oct 31	H. W. Lin et al. (2020)
9.2	spectroscopic	550–900	2019 Oct 31	H. W. Lin et al. (2020)
19.3	spectroscopic	390–600	2019 Nov 4	H. W. Lin et al. (2020)
9.2	spectroscopic	550–900	2019 Nov 4	H. W. Lin et al. (2020)
8.6 ± 2.8	...	528–860	2019 Nov 14	This work
8.1 ± 3.0	...	528–860	2019 Nov 15	This work
11 ± 0.9	photometry	330–1100	2019 Nov 24	B. Yang et al. (2021)
8.2 ± 1.6	...	528–860	2019 Nov 26	This work
18 ± 2	spectroscopy	400–500	2019 Nov 27	G. P. Prodan et al. (2024)
11 ± 1	spectroscopy	570–725	2019 Nov 27	G. P. Prodan et al. (2024)
9.9 ± 1.2	*R I*	640–790	2019 Nov 30	K. Aravind et al. (2021)
13.5 ± 1.5	*B V*	420–550	2019 Nov 30	K. Aravind et al. (2021)
5	*R I*	647–797	2019 Dec 2	E. Mazzotta Epifani et al. (2021)
9.6 ± 1.6	...	528–860	2019 Dec 5	This work
8.7 ± 1.9	...	528–860	2019 Dec 6	This work
7.1 ± 1.9	...	528–860	2019 Dec 21	This work
9.9 ± 1.2	*R I*	640–790	2019 Dec 22	K. Aravind et al. (2021)
13.5 ± 1.5	*B V*	420–550	2019 Dec 22	K. Aravind et al. (2021)
7.4 ± 1.8	...	528–860	2019 Dec 23	This work
9.9 ± 1.2	*R I*	640–790	2019 Dec 24	K. Aravind et al. (2021)
13.5 ± 1.5	*B V*	420–550	2019 Dec 25	K. Aravind et al. (2021)
11.4 ± 1.0	photometry	330–1100	2019 Dec 26	B. Yang et al. (2021)
7.6 ± 1.6	...	528–860	2019 Dec 29	This work
6.7 ± 1.7	...	528–860	2019 Dec 31	This work
7.6 ± 2.2	...	528–860	2020 Feb 2	This work
5.8 ± 4.0	...	528–860	2020 Feb 4	This work
8.9 ± 5.2	...	528–860	2020 Feb 16	This work
9.3 ± 3	photometry	330–1100	2020 Feb 19	B. Yang et al. (2021)
5.0 ± 4.1	...	528–860	2020 Feb 25	This work
4.2 ± 5.3	...	528–860	2020 Feb 28	This work
9.1 ± 1.9	...	528–860	2020 Mar 16	This work
7.9 ± 2.0	...	528–860	2020 Mar 19	This work
10.6 ± 1.4	*g*' *i*'	470–762	2019 Sep to 2020 Jan	M.-T. Hui et al. (2020)

Note. See also V. V. Busarev et al. (2021) for reflectance curves of 2I/Borisov spanning *U*, *B*, *V*, *r*, and *i*.

Appendix C
Gas Emission Maps

Appendix C contains the maps of gas emission for C_2 (Figure 12), NH_2 (Figure 13), and CN (Figure 14). Figure 15 shows the CN emission maps of Figure 14 processed by the enhancement of azimuthal median.

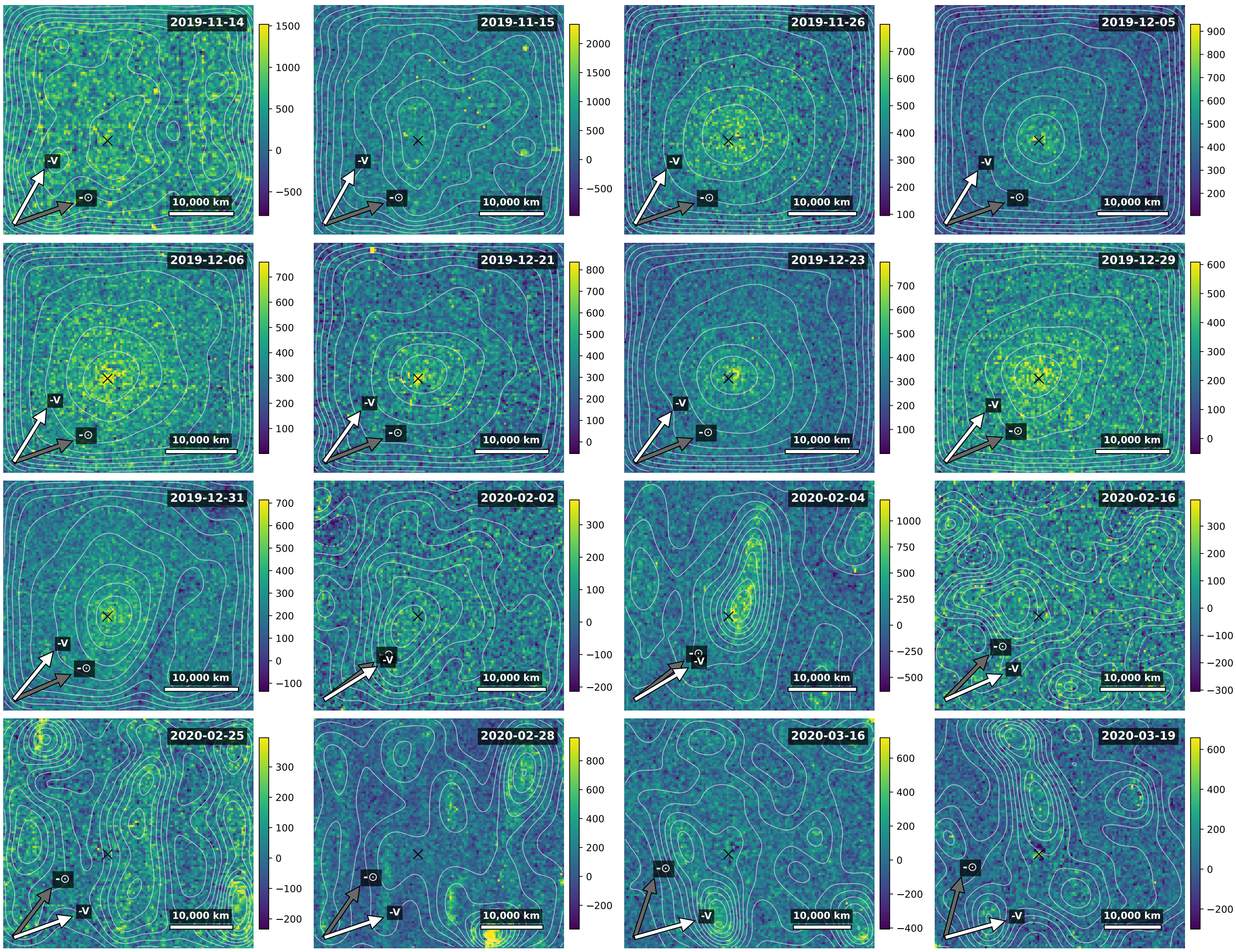

Figure 12. C_2 emission maps. Each image is centered on 2I (black cross) and displayed with a linear stretch over a zscale interval. Contour lines mark regions of equal flux and highlight when 2I was discernible above the flux of background stars for the specific wavelength range (see Table 2). North is up, east is to the left, and the antisolar (-⊙) and negative velocity ($-\boldsymbol{V}$) directions are shown with the respective arrows. The clustering of contours near the image borders is because not all exposures span the entire frame once 2I is in the center, caused by the dithering in the imaging technique, resulting in fewer frames contributing to the coadd along the borders.

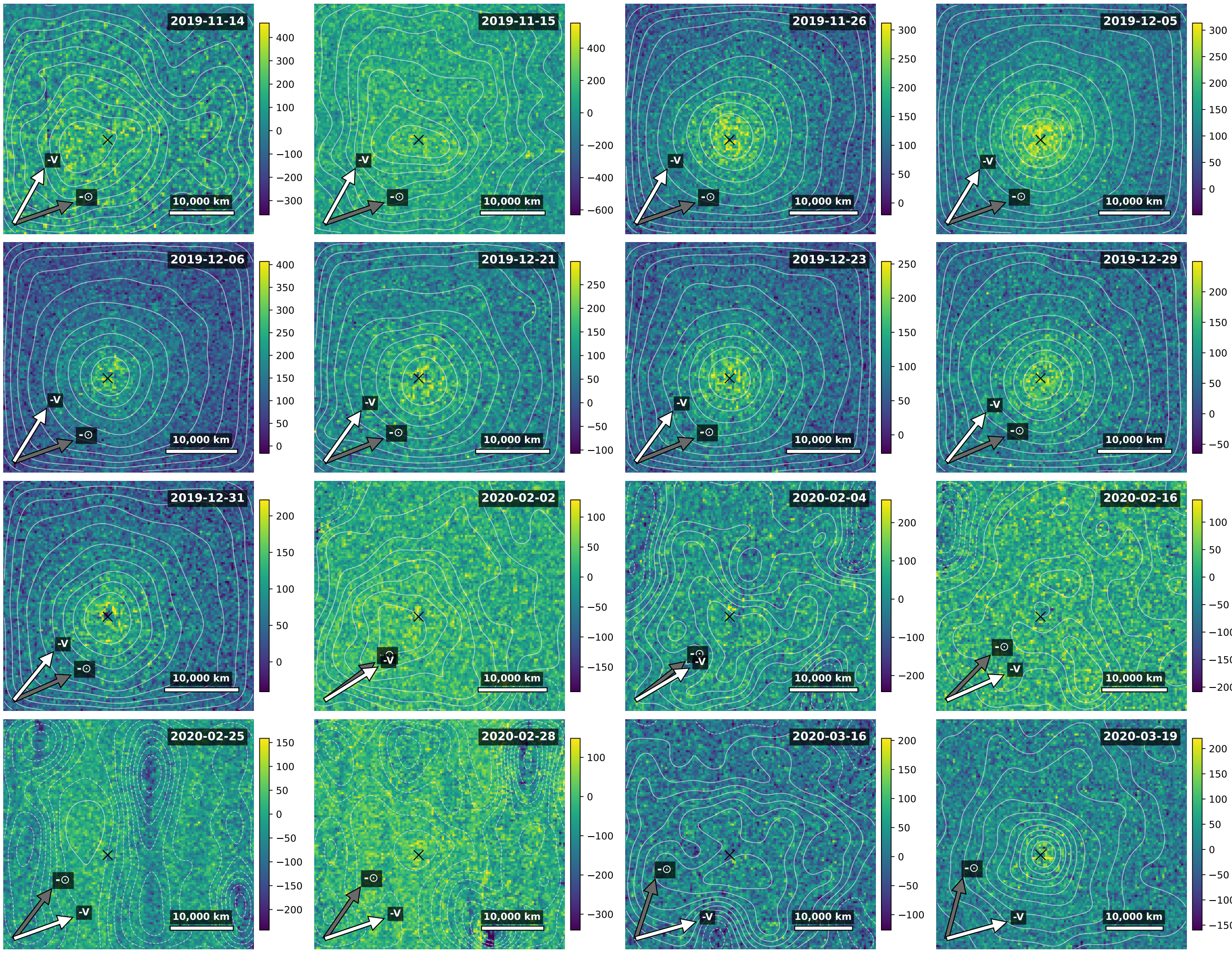

Figure 13. NH_2 emission maps. Details are the same as Figure 12.

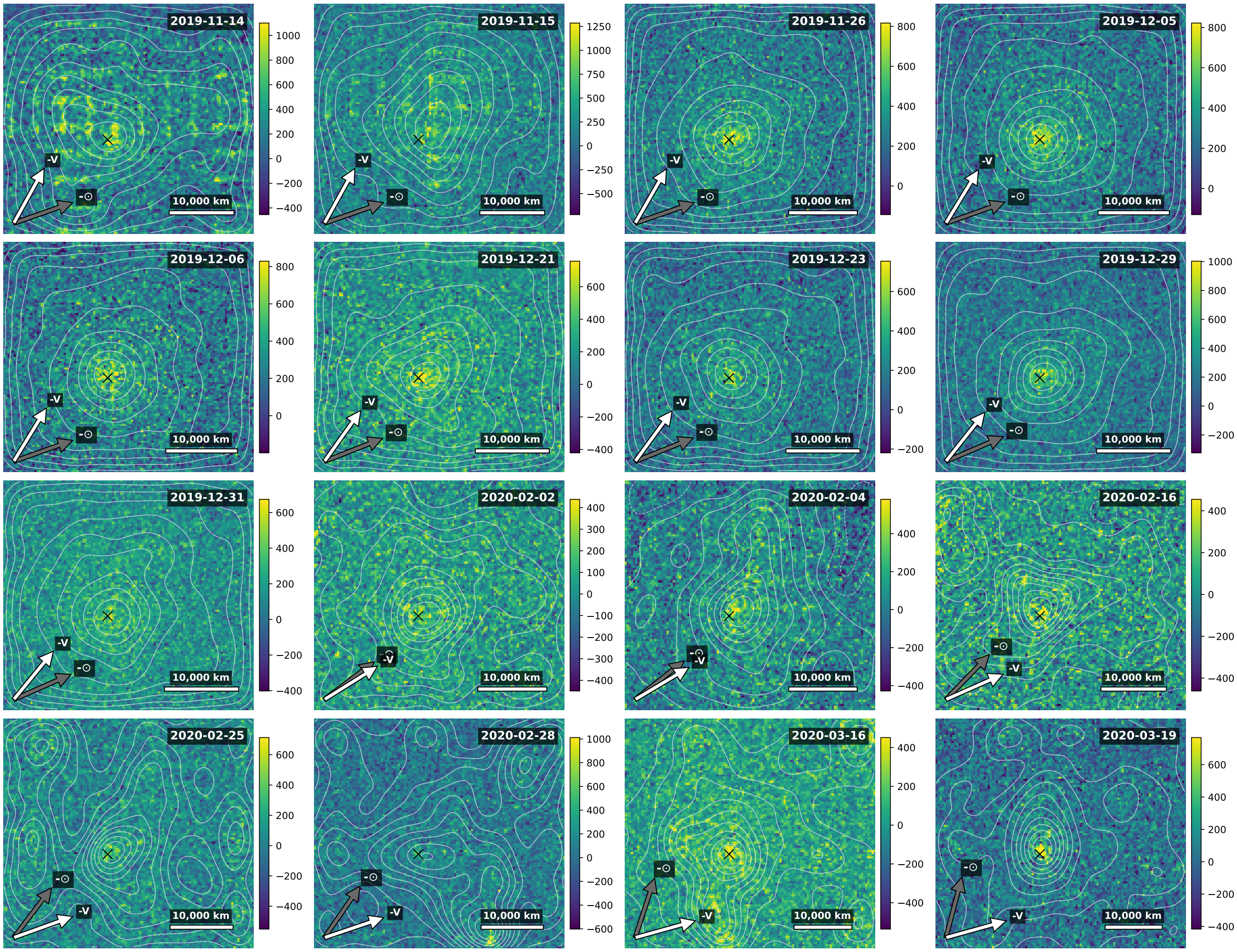

Figure 14. CN emission maps. Details are the same as Figure 12.

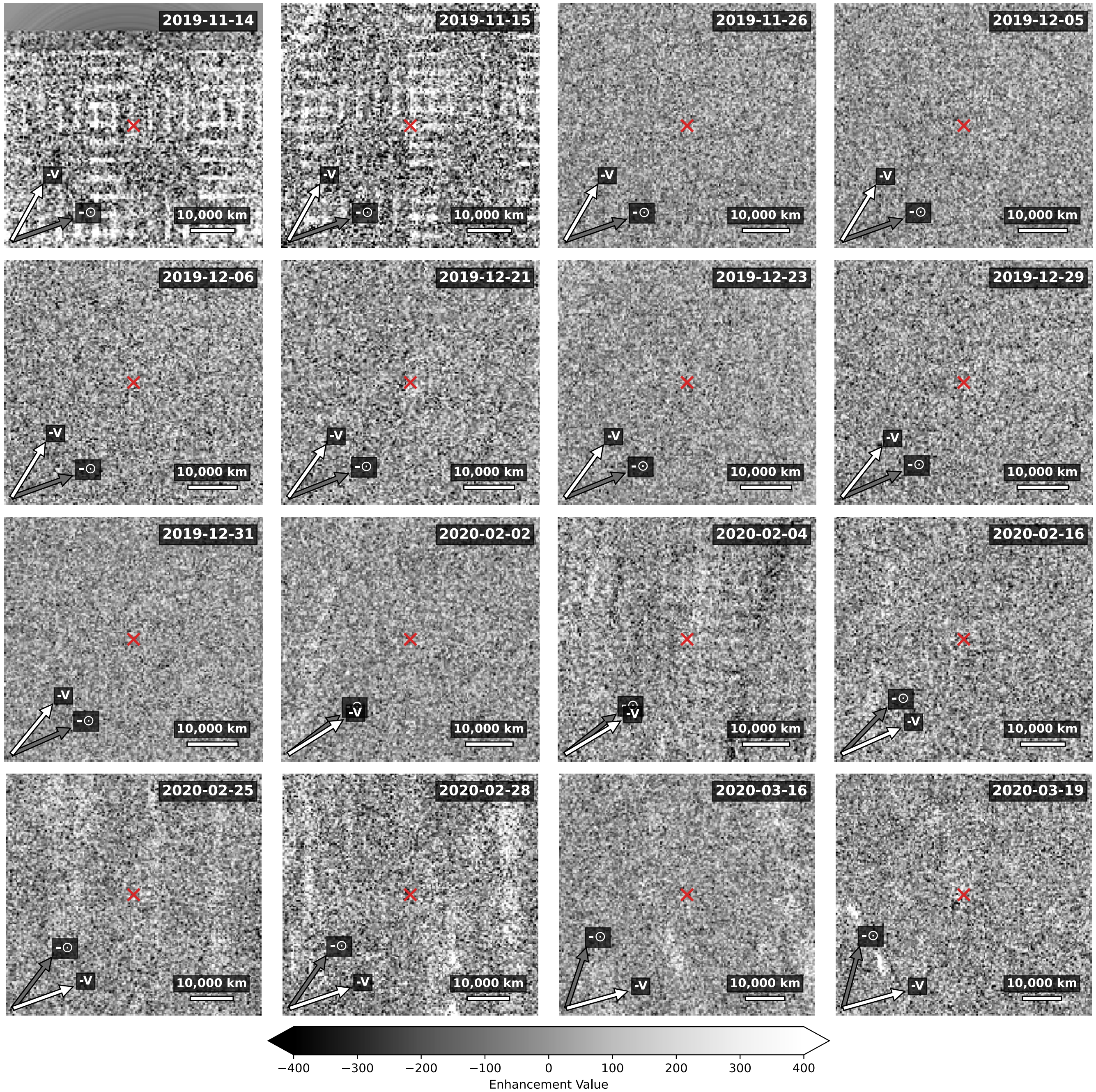

Figure 15. CN emission maps enhanced by the subtraction of the azimuthal median. Details are the same as Figure 12. The position of 2I is indicated by the red cross. The featureless images indicate uniform CN emission around the optocentre. The criss-cross pattern is an artifact from the IFU borders when fewer than four exposures were coadded.

ORCID iDs

Sophie E. Deam https://orcid.org/0000-0003-1955-628X
Michele T. Bannister https://orcid.org/0000-0003-3257-4490
Cyrielle Opitom https://orcid.org/0000-0002-9298-7484
Matthew M. Knight https://orcid.org/0000-0003-2781-6897
Léa Ferellec https://orcid.org/0000-0002-2088-3889
Ryan Ridden-Harper https://orcid.org/0000-0003-1724-2885
Darryl Z. Seligman https://orcid.org/0000-0002-0726-6480
Alan Fitzsimmons https://orcid.org/0000-0003-0250-9911
Aurélie Guilbert-Lepoutre https://orcid.org/0000-0003-2354-0766
Emmanuel Jehin https://orcid.org/0000-0001-8923-488X
Laurent Jorda https://orcid.org/0000-0001-8735-3308
Michael Marsset https://orcid.org/0000-0001-8617-2425
Youssef Moulane https://orcid.org/0000-0001-9784-6886
Philippe Rousselot https://orcid.org/0000-0001-6798-7805
Pierre Vernazza https://orcid.org/0000-0002-2564-6743
Bin Yang https://orcid.org/0000-0002-5033-9593

References

A'Hearn, M. F., Millis, R. C., Schleicher, D. O., Osip, D. J., & Birch, P. V. 1995, Icar, 118, 223
Aravind, K., Ganesh, S., Venkataramani, K., et al. 2021, MNRAS, 502, 3491
Arpigny, C. 1994, AIPC, 312, 205
Astropy Collaboration, Price-Whelan, A. M., Lim, P. L., et al. 2022, ApJ, 935, 167

Bacon, R., Piqueras, L., Conseil, S., Richard, J., & Shepherd, M. 2016, MPDAF: MUSE Python Data Analysis Framework, Astrophysics Source Code Library, ascl:1611.003
Bacon, R., Accardo, M., Adjali, L., et al. 2010, SPIE, 7735, 773508
Bagnulo, S., Cellino, A., Kolokolova, L., et al. 2021, NatCo, 12, 1797
Bair, A. N., & Schleicher, D. G. 2025, PSJ, 6, 248
Bannister, M. T., Opitom, C., Fitzsimmons, A., et al. 2020, arXiv:2001.11605
Bannister, M. T., Schwamb, M. E., Fraser, W. C., et al. 2017, ApJ, 851, L38
Biver, N., Bockelée-Morvan, D., Paubert, G., et al. 2018, A&A, 619, A127
Bodewits, D., Noonan, J. W., Feldman, P. D., et al. 2020, NatAs, 4, 867
Boehnhardt, H. 2004, in Comets II, ed. M. C. Festou, H. U. Keller, & H. A. Weaver, 301 (Univ. Arizona Press)
Bolin, B. T., & Lisse, C. M. 2020, MNRAS, 497, 4031
Bradley, L., Sipőcz, B., Robitaille, T., et al. 2023, astropy/photutils: 1.8.0, v1.8.0, Zenodo, doi:10.5281/zenodo.7946442
Busarev, V. V., Petrova, E. V., Shcherbina, M. P., et al. 2021, MNRAS, 502, 1882
Childs, A. C., & Martin, R. G. 2022, ApJL, 935, L31
Cochran, A. L., Barker, E. S., & Gray, C. L. 2012, Icar, 218, 144
Cordiner, M. A., Milam, S. N., Biver, N., et al. 2020, NatAs, 4, 861
de León, J., Licandro, J., de la Fuente Marcos, C., et al. 2020, MNRAS, 495, 2053
de León, J., Licandro, J., Serra-Ricart, M., et al. 2019, RNAAS, 3, 131
Dello Russo, N., Vervack, R. J., Weaver, H. A., et al. 2007, Natur, 448, 172
Dorsey, R. C., Hopkins, M. J., Bannister, M. T., et al. 2025, PSJ, 6, 214
Drahus, M., Guzik, P., Udalski, A., et al. 2020, ATel, 13549, 1
Farnham, T. L. 2009, P&SS, 57, 1192
Farnham, T. L., Schleicher, D. G., & A'Hearn, M. F. 2000, Icar, 147, 180
Ferellec, L., Opitom, C., Donaldson, A., et al. 2024, MNRAS, 534, 1816
Fink, U. 2009, Icar, 201, 311
Fitzsimmons, A., Hainaut, O., Meech, K. J., et al. 2019, ApJL, 885, L9
Fitzsimmons, A., Meech, K., Matrà, L., & Pfalzner, S. 2024, in Comets III, ed. K.J. Meech et al. (Univ. Arizona Press)
Fitzsimmons, A., Snodgrass, C., Rozitis, B., et al. 2018, NatAs, 2, 133
Forbes, J. C., Bannister, M. T., Lintott, C., et al. 2025, ApJ, 988, 121
Ginsburg, A., Sipőcz, B. M., Brasseur, C. E., et al. 2019, AJ, 157, 98
Gkotsinas, A., Nesvorný, D., Guilbert-Lepoutre, A., Raymond, S. N., & Kaib, N. 2024, PSJ, 5, 243
Guilbert-Lepoutre, A., Besse, S., Snodgrass, C., & Yang, B. 2016, AAS/DPS Meeting, 48, 116.12
Guzik, P., & Drahus, M. 2021, Natur, 593, 375
Guzik, P., Drahus, M., Rusek, K., et al. 2020, NatAs, 4, 53
Halder, P., & Sengupta, S. 2023, ApJ, 947, 1
Hands, T. O., Dehnen, W., Gration, A., Stadel, J., & Moore, B. 2019, MNRAS, 490, 21
Harris, C. R., Millman, K. J., van der Walt, S. J., et al. 2020, Natur, 585, 357
Haser, L. 1957, BSRSL, 43, 740
Hopkins, M. J., Bannister, M. T., & Lintott, C. 2025, AJ, 169, 78
Hui, M.-T., Ye, Q.-Z., Föhring, D., Hung, D., & Tholen, D. J. 2020, AJ, 160, 92
Hunter, J. D. 2007, CSE, 9, 90
Jewitt, D., Kim, Y., Mutchler, M., et al. 2020, ApJL, 896, L39
Jewitt, D., & Luu, J. 2019, ApJL, 886, L29
Jewitt, D., & Meech, K. J. 1986, ApJ, 310, 937
Jewitt, D., & Seligman, D. Z. 2023, ARA&A, 61, 197
Kareta, T., Andrews, J., Noonan, J. W., et al. 2020, ApJL, 889, L38
Kim, Y., Jewitt, D., Mutchler, M., et al. 2020, ApJL, 895, L34
Knight, M. M., & Schleicher, D. G. 2013, Icar, 222, 691
Knight, M. M., Snodgrass, C., Vincent, J.-B., et al. 2017, MNRAS, 469, S661
Langland-Shula, L. E., & Smith, G. H. 2011, Icar, 213, 280
Levine, W. G., Taylor, A. G., Seligman, D. Z., et al. 2023, PSJ, 4, 124
Lin, H. W., Lee, C.-H., Gerdes, D. W., et al. 2020, ApJL, 889, L30
Manoharan, P. K., Perillat, P., Salter, C. J., et al. 2022, PSJ, 3, 266
Manzini, F., Oldani, V., Ochner, P., & Bedin, L. R. 2020, MNRAS, 495, L92
Mashchenko, S. 2019, MNRAS, 489, 3003
Mazzotta Epifani, E., Dotto, E., Perna, D., et al. 2021, P&SS, 208, 105341
McKay, A., Opitom, C., Jehin, E., et al. 2024, AAS/DPS Meeting, 56, 301.01
Meftah, M., Damé, L., Bolsée, D., et al. 2018, A&A, 611, A1
Micheli, M., Farnocchia, D., Meech, K. J., et al. 2018, Natur, 559, 223
Miotello, A., Kamp, I., Birnstiel, T., Cleeves, L. C., & Kataoka, A. 2023, ASPC, 534, 501
Moro-Martín, A. 2023, in Planetary Systems Now, ed. L. M. Lara & D. Jewitt (World Scientific)
Morris, B. M., Tollerud, E., Sipőcz, B., et al. 2018, AJ, 155, 128
Mueller, B. E. A., Samarasinha, N. H., Farnham, T. L., & A'Hearn, M. F. 2013, Icar, 222, 799
Opitom, C., Guilbert-Lepoutre, A., Besse, S., Yang, B., & Snodgrass, C. 2020, A&A, 644, A143
Opitom, C., Fitzsimmons, A., Jehin, E., et al. 2019b, A&A, 631, L8
Opitom, C., Jehin, E., Manfroid, J., et al. 2015, A&A, 574, A38
Opitom, C., Yang, B., Selman, F., & Reyes, C. 2019a, A&A, 628, A128
Opitom, C., Jehin, E., Hutsemékers, D., et al. 2021, A&A, 650, L19
'Oumuamua ISSI Team, Bannister, M. T., Bhandare, A., et al. 2019, NatAs, 3, 594
pandas development team T. 2020, pandas-dev/pandas: Pandas, latest, v3.0.1, Zenodo, doi:10.5281/zenodo.3509134
Pfalzner, S., Aizpuru Vargas, L. L., Bhandare, A., & Veras, D. 2021, A&A, 651, A38
Portegies Zwart, S. 2021, A&A, 647, A136
Portegies Zwart, S., Torres, S., Pelupessy, I., Bédorf, J., & Cai, M. X. 2018, MNRAS, 479, L17
Prodan, G. P., Popescu, M., Licandro, J., et al. 2024, MNRAS, 529, 3521
Raymond, S. N., Armitage, P. J., Veras, D., Quintana, E. V., & Barclay, T. 2018, MNRAS, 476, 3031
Rhodes, B. C. 2011, PyEphem: Astronomical Ephemeris for Python, Astrophysics Source Code Library, ascl:1112.014
Ridden-Harper, R., Bannister, M. T., Deam, S. E., & Nordlander, T. 2025, AJ, 169, 148
Schleicher, D. G., & Bair, A. N. 2011, AJ, 141, 177
Seabold, S., & Perktold, J. 2010, in 9th Python in Science Conf.
Seligman, D. Z., & Moro-Martín, A. 2023, ConPh, 63, 200
Shinnaka, Y., Kawakita, H., Kondo, S., et al. 2017, AJ, 154, 45
Smette, A., Sana, H., Noll, S., et al. 2015, A&A, 576, A77
Tegler, S., & Wyckoff, S. 1989, ApJ, 343, 445
Villanueva, G. L., Smith, M. D., Protopapa, S., Faggi, S., & Mandell, A. M. 2018, JQSRT, 217, 86
Virtanen, P., Gommers, R., Oliphant, T. E., et al. 2020, NatMe, 17, 261
Weilbacher, P. M., Palsa, R., Streicher, O., et al. 2020, A&A, 641, A28
McKinney, W. 2010, in Proc. of the 9th Python in Science Conf., ed. S. van der Walt & J. Millman, 56
Williams, G. V., Sato, H., Sarneczky, K., et al. 2017, CBET, 4450, 1
Xing, Z., Bodewits, D., Noonan, J., & Bannister, M. T. 2020, ApJL, 893, L48
Yang, B., Kelley, M. S. P., Meech, K. J., et al. 2020, A&A, 634, L6
Yang, B., Li, A., Cordiner, M. A., et al. 2021, NatAs, 5, 586
Ye, Q., Kelley, M. S. P., Bolin, B. T., et al. 2020, AJ, 159, 77